JACS
JOURNAL OF THE AMERICAN CHEMICAL SOCIETY
Article
pubs.acs.org/JACS

Spectroscopic and DFT Studies of Second-Sphere Variants of the Type 1 Copper Site in Azurin: Covalent and Nonlocal Electrostatic Contributions to Reduction Potentials

Ryan G. Hadt,[†] Ning Sun,[†] Nicholas M. Marshall,[‡] Keith O. Hodgson,[†,§] Britt Hedman,[§] Yi Lu,*[,‡] and Edward I. Solomon*[,†,§]

[†]Department of Chemistry, Stanford University, Stanford, California 94305, United States

[§]Stanford Synchrotron Radiation Lightsource, SLAC National Accelerator Laboratory, Stanford University, Menlo Park, California 94025, United States

[‡]Department of Chemistry, University of Illinois at Urbana−Champaign, Illinois 61801, United States

Supporting Information

ABSTRACT: The reduction potentials (E^0) of type 1 (T1) or blue copper (BC) sites in proteins and enzymes with identical first coordination spheres around the redox active copper ion can vary by ∼400 mV. Here, we use a combination of low-temperature electronic absorption and magnetic circular dichroism, electron paramagnetic resonance, resonance Raman, and S K-edge X-ray absorption spectroscopies to investigate a series of second-sphere variants—F114P, N47S, and F114N in *Pseudomonas aeruginosa* azurin—which modulate hydrogen bonding to and protein-derived dipoles nearby the Cu−S(Cys) bond. Density functional theory calculations correlated to the experimental data allow for the fractionation of the contributions to tuning E^0 into covalent and nonlocal electrostatic components. These are found to be significant, comparable in magnitude, and additive for active H-bonds, while passive H-bonds are mostly nonlocal electrostatic in nature. For dipoles, these terms can be additive to or oppose one another. This study provides a methodology for uncoupling covalency from nonlocal electrostatics, which, when coupled to X-ray crystallographic data, distinguishes specific local interactions from more long-range protein/active interactions, while affording further insight into the second-sphere mechanisms available to the protein to tune the E^0 of electron-transfer sites in biology.

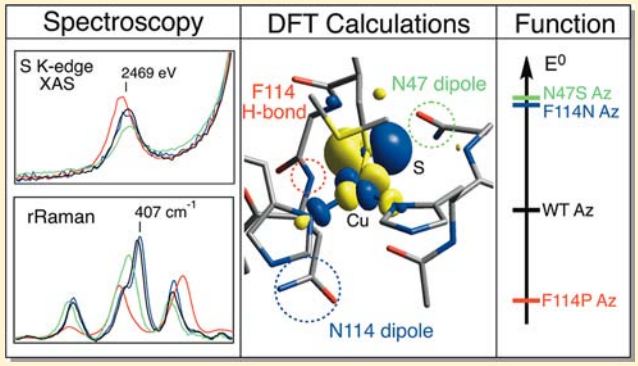

1. INTRODUCTION

Blue copper (BC), or type 1 (T1) copper proteins,[1] mediate long-range, rapid, and directional electron transfer (ET) in a variety of biological functions.[2−5] The geometric structure of this active site consists of a conserved equatorial trigonal ligand field (LF) made up of a very short Cu−S(Cys) bond and two Cu−N(His) bonds.[6−8] There are two axial ligand positions. The *syn* (to the C_β−S(Cys) bond) position can be occupied by S(Met) (e.g., plastocyanin (Pc)[8] and azurin (Az)[9]), O(Gln) (e.g., stellacyanin[10]), or nothing (Ile/Phe) (e.g., fungal laccases[11,12]). The *trans*-axial position can be occupied by a carbonyl group provided by the protein backbone (as in Az), which does not covalently bond to Cu but does contribute electrostatically,[13] or nothing (e.g., Pc and fungal laccases).

The BC proteins have been studied intensely due to their unique spectral features.[14−16] For the classical BC proteins these consist of an intense S(Cys)→Cu^{2+} ligand-to-metal charge-transfer (LMCT) transition at ∼600 nm ($\varepsilon \approx 5000$ $M^{-1}cm^{-1}$),[17] which imparts the characteristic blue color, and a small parallel ^{63,65}Cu hyperfine coupling ($A_\parallel$).[18,19] These unique spectral features reflect the high anisotropic covalency of the T1 site due to the strong π overlap between the Cu($3d_{x^2-y^2}$) orbital and the out-of-(Cu−S−C_β)-plane S(3p) orbital. This forms the redox-active molecular orbital (RAMO), which is strongly delocalized over both the Cu and the S(thiolate) ligand (Figure 1).

For their ET function, a key property of the BC proteins is their reduction potential (E^0). It has been demonstrated previously that, within the first coordination sphere of the T1 site, the *trans*-axial ligand plays a major role in tuning E^0.[20−23] Through analyses of site-directed axial ligand mutants of the T1 site, it was found that E^0 had a positive linear correlation with the hydrophobicity of the axial ligand.[20,21] Also, through the analyses of the temperature dependence of the absorption and resonance Raman (rR) spectra of the native T1 site in green nitrite reductase combined with density functional theory (DFT) calculations, it was determined that the S(Met) thioether ligand can tune E^0 down by ∼200 mV due to a stronger interaction energy with the oxidized than the reduced

Received: July 7, 2012
Published: September 18, 2012

   dx.doi.org/10.1021/ja306438n | J. Am. Chem. Soc. 2012, 134, 16701−16716

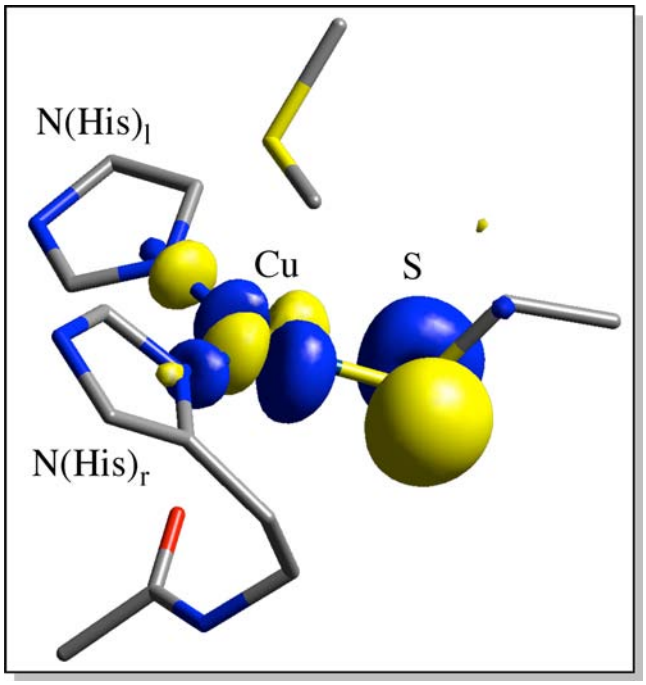

Figure 1. β-LUMO of the T1 site. Atoms: Cu, labeled with text; S, yellow; N, blue; O, red; and C, gray.

state.[23] The constraint of the Cu−S(Met) distance during redox cycling represents the entatic/rack nature[24−26] of the T1 active site.[23] In addition to the influence of the axial ligand, T1 sites with identical active site ligation can have a wide range of reduction potentials (>400 mV).[15,27] As with other ET proteins, the outer-sphere environment is a significant determinant of E^0 as well, capable of tuning it over this large potential range.

A variety of experimental and computational studies have focused on elucidating the role of outer-sphere protein/solvent (defined here as H_2O) interactions with the active site on the E^0 of BC proteins.[27−34] Parallel studies have also been performed on other redox proteins.[35−40] While the growing body of data has led to the development of concepts for understanding outer-sphere mechanisms available to ET proteins to tune E^0, this is still a difficult endeavor, mostly due to the complexity involved in distinguishing between contributions that can potentially compensate. At least for BC proteins, the mechanism of outer-sphere tuning of E^0 has been considered largely electrostatic in origin, with less focus on contributions from the effects on the covalency of the sulfur−metal bond (defined here as the amount of S(ligand) character present in the redox active metal $3d_{x^2-y^2}$ of the BC site in Figure 1). Experiment[27,41−45] and DFT calculations[28] have indicated that H-bonding to the S(Cys) ligand increases E^0. Likewise, by means of DFT calculations[28] and site-directed mutagenesis,[27,46−48] negatively oriented dipoles have been shown to decrease the potential of the T1 site. The effects of hydrophobicity of the axial position on E^0 have also been extended to the outer-sphere environment.[32] However, it is important to note that these factors (H-bonds, dipoles, and hydrophobicity) can change the covalency of the ligand−metal bond as well as make electrostatic contributions that do not impact the ligand−metal covalency. Furthermore, H-bonds and protein dipoles have orientations that can have differential effects on the covalency and electrostatics. Thus, to understand outer-sphere protein contributions to tuning E^0, it is important to uncouple and separately estimate the electrostatic contributions and the effects of the protein environment on the covalency of the active site. It is also important to further understand how these are affected by specific H-bond and dipole orientations. This is the focus of the present study.

Recent experimental and computational studies on FeS proteins have been directed toward estimating the covalent contribution[39,49] to E^0 as well as uncoupling the role of solvent accessibility to the active site.[38,50] Differences in ligand−metal covalency were found to be major contributors to the differences in E^0. A few computational studies related to understanding the role of the outer-sphere environment in BC and FeS proteins have allowed for the protein and solvent to polarize the solute,[30,37,51] which is akin to changes in ligand−metal covalency; however, the contributions from electrostatics and ligand−metal covalency were not uncoupled. The decomposition of covalent and electrostatic contributions thus represents a significant goal in understanding the influence of the outer-sphere environment on the E^0 of ET sites in biology, and, more broadly, for the rational design of redox active components in catalytic architectures.

In the present study, we have used a variety of spectroscopic methods and DFT calculations correlated to experiment in order to investigate the BC sites of the second-sphere variants of Az in Table 1. Systematic variations in E^0 by ∼225 mV at the same pH have been measured for this series of second-sphere variants,[27] which maintain identical first coordination sphere ligand sets. The three variants modulate E^0: (1) F114P Az eliminates an H-bond to the S(Cys) of the BC site;[41] (2) N47S Az deletes a carbonyl dipole that is at a distance of ∼3.5 Å for the S(Cys) ligand;[27] and (3) F114N Az inserts a carbonyl dipole ∼5.0 Å from Cu[27] (Figure 2). These studies allow the

Table 1. E^0 for WT Az and the Variants at pH 7

protein	E^0 (mV)[a]
WT Az	265 ± 19
F114P Az	171 ± 7
N47S Az	396 ± 26
F114N Az	394 ± 4

[a]Reference 27.

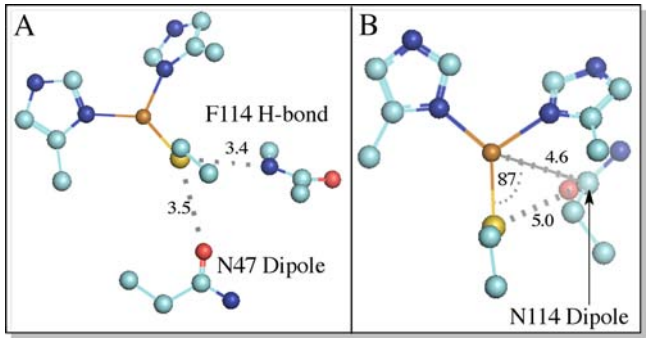

Figure 2. Position of second-sphere residue/Cu−S(Cys) interactions. (A) F114 H-bond and N47 dipole and (B) the N114 dipole (distances are measured to the C atom of the carbonyl group; the angle is measured between S(Cys)−Cu−C(O)). For clarity, the axial S(Met) ligand is not shown. Atoms: Cu, brown; S, yellow; N, blue; O, red; and C, teal.

dx.doi.org/10.1021/ja306438n | J. Am. Chem. Soc. 2012, 134, 16701−16716

effect of the environment on E^0 to be uncoupled by determining that these changes in the environment around the BC center both change the covalency of the Cu−S(Cys) bond as well as make nonlocal electrostatic contributions (defined here as having no associated change in covalency) to E^0. The covalent component is obtained directly from experiment (S K-edge X-ray absorption spectroscopy (XAS)), allowing for the independent evaluation of the two contributions. They further have different orientation dependencies for H-bonds and carbonyl dipoles. The experimental quantification and fractionation of these terms provides insight into how the second sphere of the protein tunes the E^0 of T1 copper proteins and, in general, ET sites in biology.

2. MATERIALS AND METHODS

2.1. Protein Expression and Purification. Expression and purification of WT *Pseudomonas aeruginosa* Az and the variants studied here were performed using previously published protocols.[27,52,53]

2.2. Electronic Absorption and Magnetic Circular Dichroism (MCD) Spectroscopy. Low-temperature (LT) absorption spectroscopy was performed using a Cary 500 double-beam spectrophotometer modified with a Janis Research Super Vari-Temp liquid helium cryostat mounted in the optical path. LT MCD experiments were conducted using two Jasco spectropolarimeters. Each is equipped with a modified sample compartment to accommodate focusing optics and an Oxford Instruments SM4000-7T superconducting magnet/cryostat. This arrangement allows data collection at temperatures from 1.6 to 290 K and fields up to 7 T. A Jasco J810 spectropolarimeter operating with an S-20 photomultiplier tube was used to access the visible and ultraviolet spectral region. A Jasco J730 spectropolarimeter operating with a cooled InSb detector was used for the near-infrared region. MCD samples (50/50 v/v buffer/glycerol mixture) were made in cells fitted with quartz disks and a 0.2 cm rubber gasket spacer. Simultaneous Gaussian fitting of the absorption and MCD spectra was performed with the Peak-Fit program (Jandel).

2.3. Electron Paramagnetic Resonance (EPR) Spectroscopy. X-band EPR spectra were obtained using a Bruker EMX spectrometer. X-band spectra were obtained at 77 K in a liquid nitrogen finger dewar using an ER 041 XG microwave bridge and an ER 4102ST cavity (parameters for recording the X-band EPR data: 9.39 GHz frequency and 10 G modulation amplitude). Protein concentrations for the EPR spectra were ∼1 mM. X-band data were simulated using the XSophe program.

2.4. Resonance Raman (rR) Spectroscopy. Resonance Raman spectra were obtained in an ∼135° backscattering configuration with an incident power of ∼20 mW using either a Coherent I90C-K Kr^+ CW ion laser (for WT, N47S, and F114N Az protein samples a the 647.1 nm laser line was used as the excitation source) or a dye laser (Rhodamine 6G, Coherent 599) pumped by a Coherent Innova Sabre 25/7 Ar^+ CW ion laser (for the F114P Az protein sample a 600.0 nm laser line was used as the excitation source). Scattered light was dispersed through a triple monochromator (Spex 1877 CP, with 1200, 1800, and 2400 groove/mm gratings) and detected with an Andor Newton charge-coupled device (CCD) detector cooled to −80 °C. Samples were contained in NMR tubes immersed in a liquid nitrogen finger dewar. Background spectra were obtained using charcoal at 77 K in an NMR tube. Raman energies were calibrated using Na_2SO_4 and citric acid. Frequencies are accurate to within 2 cm^{-1}.

2.5. S K-Edge X-ray Absorption Spectroscopy (XAS). S K-edge spectra were measured at the Stanford Synchrotron Radiation Lightsource (SSRL) using the 54-pole wiggler beamline 4-3. Details of the optimization of this beamline for low-energy fluorescence measurements and the experimental setup have been described previously.[54] S K-edge measurements were performed at ∼4 °C. Protein samples were pre-equilibrated in a water-saturated He atmosphere for ∼0.5−1 h to minimize bubble formation in the sample cell. Protein solutions were loaded via syringe into a Pt-coated Al block sample holder with a 6.35 μm thick polypropylene window. Prior to beam exposure, all protein samples were fully oxidized using 10-fold excess K_3FeCN_6[55] and were monitored for potential effects of photoreduction throughout the course of data collection. 3−5 scan averages were obtained with no indication of photoreduction. The energy was calibrated from S K-edge spectra of $Na_2S_2O_3{\cdot}5H_2O$ (first pre-edge feature at 2472.02 eV), run at intervals between sample scans. Data normalization was performed as described in earlier publications.[56] All samples were spin quantified by EPR using a copper standard to determine the active site loading. The area under the pre-edge peak was quantified by fitting the data using EDG_FIT.[57] The pre-edge and rising-edge features were modeled with pseudo-Voigt line-shapes with a fixed 1:1 Lorentzian/Gaussian ratio. Normalization procedures introduce ∼3% error in the value of the integrated area under the pre-edge peak. The fitted intensities were converted to % S(3p) character using the pre-edge feature of Pc as a reference (where 1.02 units of intensity, obtained using EDG_FIT, corresponded to 38% S(3p) character).

2.6. Density Functional Theory (DFT) Calculations. All calculations were carried out using the Gaussian 09 program.[58] Properties calculations (i.e., population analyses and ionization energy (IE) calculations) were carried out using solvent corrections (PCM, ε = 4.0).[59] All IEs are adiabatic (i.e., difference in energy between optimized oxidized and reduced states). All molecular orbital compositions were determined using the QMForge program[60] (c^2 and Mulliken population analyses), and all orbital surfaces were generated using the β-LUMO program.[61] Gas phase TDDFT calculations were visualized using the SWizard program revision 4.6[62,63] using Gaussian band-shapes with half-widths of 2500 cm^{-1}. Several different structural models were utilized in the different Results and Analysis subsections.

For section 3.2.1, all calculations were carried out using the B3LYP[64] exchange correlation functional (spin unrestricted) with a split-valence basis set (Cu (triple-ζ TZVP[65]) S (6-311G(d)) and all other atoms (6-31G(d)[66−68]). Both large and a small models of WT Az have been partially geometry optimized. (**L-WT** and **S-WT**, respectively (see Supporting Information Figure S1 for **L**- and **S**-type structures). The starting point for optimization of **L-WT** was derived from X-ray crystallographic coordinates (PDB ID: 1JZF[5]). Note that crystallographic resolutions are given below in Tables 6−8. **L-WT** contains the second-sphere protein backbone and side chain R-groups relevant for this study (i.e., F114 and N47; Figure 2). **L-WT** was partially geometry optimized with protein backbone and R-group constraints (i.e., α- and β-carbons, amide N's, carbonyl O's, and terminal methyl C's). **S-WT** is a truncated version of **L-WT** and contains only the side chain R-groups and an ethyl thiolate (S(Et)), which has been used in place of the full S(Cys) of **L-WT**. The amide H-bonds to the S(Et) ligand in **S-WT** are modeled with H−F molecules. Note that H−F was chosen due to the similarity of its dipole moment with that of the H−N unit of the amide backbone (e.g., the dipole moment of acetamide is 3.44 D (solvent is benzene), with estimated bond moments for the C═O, N−H, C−N, and C−CH_3 units of 2.4, 0.4, 1.3, and 0.4 D, respectively).[69] Partial geometry optimization of **S-WT** involved constraining the α- and β-carbons and the second-sphere R-groups in their X-ray crystallographic positions. The **S-WT** model allows for the systematic perturbation of side chain residues and H-bonds to the S(thiolate) ligand and facilitates further correlation to spectroscopic data with TDDFT and frequency calculations.

Analogous to **L-WT**, a large model for partial geometry optimization of the F114P Az variant (**L-F114P**) was created from the X-ray crystallographic coordinates of the oxidized form (PDB ID: 2GHZ[41]). The small F114P Az model (**S-F114P**) was constructed by simply removing one H−F molecule from **S-WT** followed by a partial reoptimization of the structure with identical constraints.

X-ray crystal structures do not exist for the N47S and F114N Az single mutants; however, an N47S/F114N Az double mutant X-ray crystal structure does exist (PDB ID: 3JTB[27]). The large model for N47S Az (**L-N47S**) was obtained by removing the N47 residue from **L-WT** and reoptimizing the structure, while the large F114N Az model

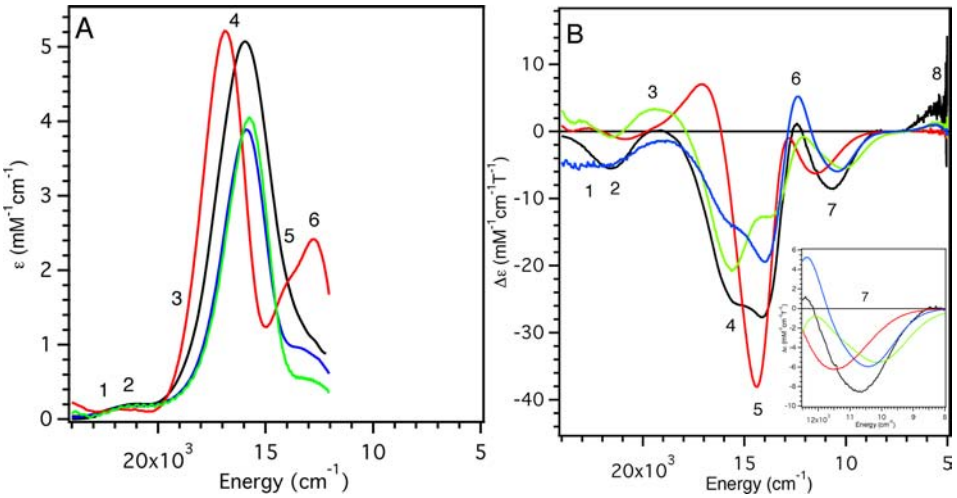

Figure 3. (A) LT (5 K) electronic absorption and (B) MCD (5 K, 5 T) spectra of WT Az (black line), F114P Az (red line), N47S Az (green line) and F114N Az (blue line). Inset: expanded portion of the MCD spectra in the energy region of band 7.

(**L-F114N**) was created by replacing the F114 R-group with N114 using the N114 X-ray crystallographic coordinates from the N47S/F114N Az double mutant. It should be noted that in an overlay of the WT Az and N47S/F114N Az X-ray crystal structures the F114 and N114 R-groups are nearly congruent; however, the orientation of the Asn carbonyl dipole cannot be determined from X-ray crystallography. Investigation of the H-bonding partners surrounding the R-group as well as partial geometry optimization of an extended F114N Az model, which contained all potential H-bonding donors and acceptors in the vicinity of the N114 residue, resulted in a preferred orientation (by ∼3 kcal/mol). This orientation has the positive side of the dipole closest to Cu (see Supporting Information Figure S2). The small N47S Az model (**S-N47S**) was constructed by deletion of the N47 R-group from **S-WT** followed by reoptimizing the structure. The small F114N Az model (**S-F114N**) was created by replacing the Phe114 ring of **S-WT** with Asn114 in a manner identical to **L-F114N**.

For section 3.2.2, all calculations were carried out using the B(38HF)P86[64,70−72] functional (spin unrestricted) with the same split-valence basis set as in section 3.2.1. For all calculations the T1 geometry is $Cu^{(2+/+)}(S(Et))(S(Me)_2)(N(Im))_2$ (where Et = ethyl, Me = methyl, and Im = imidazole). H-bond donors are modeled using an H−F molecule, analogous to the small models discussed above. Geometries are partially reoptimized at each H-bond distance and orientation in both oxidized and reduced states.

For section 3.2.3, all calculations were carried out in an identical manner to section 3.2.2; however, due to the large number of calculations geometries were not reoptimized at each dipole distance and orientation. Dipoles are modeled using two equal and oppositely charged point charges (0.66 and −0.66 in the Gaussian 09 program) at a distance of 1.5 Å from one another, which corresponds to a dipole moment similar in magnitude to that of a carbonyl group in the amide unit (calculated at the same level of theory).

3. RESULTS AND ANALYSIS

3.1. Spectroscopic. *3.1.1. Electronic Absorption and Magnetic Circular Dichroism.* The LT electronic absorption and MCD spectra of WT, F114P, N47S, and F114N Az are presented in Figure 3 (5000−24000 cm^{-1} region). Full Gaussian resolutions obtained from simultaneous fits of the absorption and MCD spectra are included in Supporting Information Figure S3 and are summarized in Table 2. For consistency, we adopt the numbering scheme for electronic excited states developed for Pc,[17] which is given in the Gaussian resolutions in Figure S3 and included in Figure 3.

The electronic spectral data can be divided into two regions: LF transitions and LMCT transitions. The nature of the transition was identified by its $|C_0/D_0|$ ratio (i.e., MCD relative to absorption intensity) (Table 2). The ratios were calculated using[73]

$$\frac{C_0}{D_0} = \frac{kT}{\mu_B B}\left(\frac{\Delta\varepsilon}{\varepsilon}\right)_{max} \quad (1)$$

where T is the temperature, B is the external magnetic field strength, k is Boltzmann's constant, μ_B is the Bohr magneton, ε is the absorption maximum in M^{-1} cm^{-1}, and $\Delta\varepsilon$ is the MCD intensity maximum, also measured in M^{-1} cm^{-1}. k/μ_B is ∼1.489 T K^{-1}.[74] For BC sites, the magnitude of the C-term dominantly derives from spin−orbit coupling, which reflects metal d-character and results in intense LF transitions in MCD relative to their respective absorption intensities at the same temperature.[17] This relationship allows the transitions observed in the low energy region (∼5000−13000 cm^{-1}) to be assigned as copper-centered LF transitions. They follow the energy order (from assignments for Pc[17]): $3d_{z^2}\rightarrow 3d_{x^2-y^2}$ (band 8) < $3d_{xy}\rightarrow 3d_{x^2-y^2}$ (band 7) < $3d_{xz+yz}\rightarrow 3d_{x^2-y^2}$ (band 6) < $3d_{xz-yz}\rightarrow 3d_{x^2-y^2}$ (band 5). LMCT transitions are at higher energy and assigned as the S(Cys)π (band 4), S(Cys)σ (band 3), N(His) (band 2) and the S(Met)→$Cu(3d_{x^2-y^2})$ (band 1) CT.

Upon removal of an H-bond from the S(Cys) ligand (F114P Az, Figure 3, red lines) the S(Cys)$\pi\rightarrow Cu(3d_{x^2-y^2})$ CT band (band 4) is blue-shifted by ∼900 cm^{-1} and the ε increases. Associated with the increase in ε of band 4 there is an increase in the ε of bands 5 and 6 (the $3d_{xz,yz}$ combination of LF transitions, which mix with the S(Cys)$\pi\rightarrow Cu(3d_{x^2-y^2})$ CT band). From the MCD data, the energy of the $3d_{xy}\rightarrow 3d_{x^2-y^2}$ LF transition (band 7) increases by ∼900 cm^{-1} (Figure 3B, inset). For N47S Az, removing the negatively oriented dipole from within vicinity of the S(Cys) ligand also perturbs the excited-state spectral data (green lines). Band 4 shows a small red-shift (∼200 cm^{-1}) and a decrease in ε, while bands 5 and 6 also have a decreased ε. Band 7 decreases in energy by ∼500 cm^{-1}. For F114N Az (blue lines), the electronic absorption spectrum is almost identical to WT Az, but with a decrease in the ε of band 4 and the LF transitions with which it mixes (bands 5 and 6). The energy of band 7 does not change.

dx.doi.org/10.1021/ja306438n | J. Am. Chem. Soc. 2012, 134, 16701−16716

Table 2. Experimental Electronic Absorption and MCD Parameters

band	assignments in PLC	wavenumber				ε (M^{-1} cm^{-1})				$\Delta\varepsilon$ (M^{-1} cm^{-1} T^{-1})				C_0/D_0			
		WT	F114N	F114P	N47S	WT	F114N	F114P	N47S	WT	F114N	F114P	N47S	WT	F114N	F114P	N47S
8	d_{z^2}	5430	5750		5500					+3.5	+0.9		+1.1	+	+		+
7	d_{xy}	10700	10600	11800	10200					−8.8	−6.4	−6.7	−6.1	−	−	−	−
6	d_{xz+yz}	12600	12500	13000	12500	730	750	2150	450	+16.9	+10.5	+10.0	+2.0	+0.25	+0.10	+0.03	+0.03
5	d_{xy-yz}	13700	13800	14200	13500	740	650	1400	250	−23.3	−19.0	−39.6	−5.3	−0.34	−0.22	−0.21	−0.16
4	Cys π	15900	15800	16800	15700	5070	3900	5225	4050	−19.2	−12.8	+7.1	−21.1	−0.04	−0.02	+0.01	−0.04
3	Cys σ	18100	17400	20900	16900	510	830	880	1150	+2.9	−1.5	+1.7	−2.7	+0.06	−0.01	+0.01	−0.02
2	His π	20100	19300	22200	18600	160	210	125	350	−0.8	−0.9	−1.2	+2.8	−0.05	−0.03	−0.07	+0.06
1	Met	21900	21200	24600	21200	170	150	125	250	−1.0		+0.5	−1.9	−0.06		+0.03	−0.06

Thus, the major changes observed in Figure 3 associated with the variants are: (1) shifts in energy of the d_{xy} LF transition, which will be used in the EPR analysis in the next section, and (2) variations in the energy and intensity of the S(Cys)$\pi\rightarrow$Cu($3d_{x^2-y^2}$) CT band (band 4) and its intensity mixing into the lower energy LF transitions. Generally, the energy and intensity of band 4 reflect the antibonding interaction of the Cu($3d_{x^2-y^2}$)-based β-LUMO with the S(Cys)π donor orbital: the stronger the interaction, the higher the energy and intensity of this band. Therefore, removing an H-bond to the S(Cys) ligand in F114P Az increases its antibonding interaction with the β-LUMO, as the energy and intensity of the S(Cys)$\pi\rightarrow$Cu($3d_{x^2-y^2}$) CT band (band 4) increases. Conversely, removing the negatively oriented dipole near the S(Cys) in N47S Az decreases the antibonding character of the β-LUMO, as the energy and intensity of the (Cys)$\pi\rightarrow$Cu($3d_{x^2-y^2}$) CT band (band 4) decreases. However, in F114N Az, where a dipole is added near copper, there is a decrease in intensity of band 4 with no change in energy. As shown in section 3.2.1, this effect reflects a dominant interaction of the dipole with the S(Cys)π donor rather than the acceptor β-LUMO in the CT process. Note also that residue 114 is farther from the BC center (~5 Å from Cu) than residue 47 (~3.5 Å from S) and is solvent exposed, which would lessen its effect.

3.1.2. Electron Paramagnetic Resonance. The X-band EPR spectra and their simulations for WT Az and the variants are shown in Figure 4. The resulting spin Hamiltonian parameters

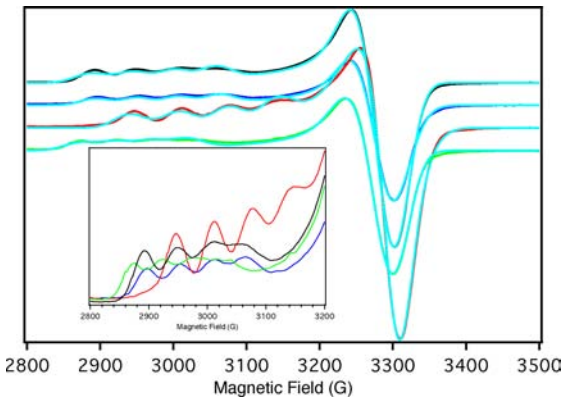

Figure 4. 77 K X-band EPR spectra of WT Az (black line), F114P Az (red line), N47S Az (green line), and F114N Az (blue line) and simulated data (turquoise). Inset: expanded $g_{\|}$ region.

are summarized in Table 3. The observation of $g_{\|} > g_{\perp} > 2.0023$ indicates that the unpaired electron is in the Cu($3d_{x^2-y^2}$) orbital. Relative to WT Az, the $g_{\perp}$ and $A_{\perp}$ ($g_{x,y}$ and $A_{x,y}$) of the variants show only small deviations; however, both $g_{\|}$ and $A_{\|}$ (g_z and A_z) do exhibit changes. For F114P Az $g_{\|}$ decreases from 2.262

Table 3. Spin Hamiltonian Parameters from Simulations of the X-Band EPR Spectra

	WT Az	F114P Az	N47S Az	F114N Az
g_x	2.042	2.044	2.040	2.042
g_y	2.056	2.046	2.061	2.055
g_z	2.262	2.211	2.283	2.258
A_x, $\times 10^{-4}$ cm^{-1}	11	6	10	11
A_y, $\times 10^{-4}$ cm^{-1}	11	13	11	11
A_z, $\times 10^{-4}$ cm^{-1}	59	68	51	58

dx.doi.org/10.1021/ja306438n | J. Am. Chem. Soc. 2012, 134, 16701−16716

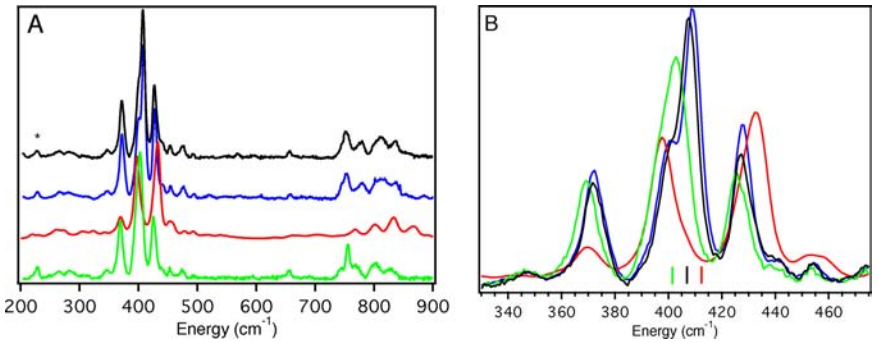

Figure 5. (A) 77 K rR spectra of WT Az (black line, 647.1 nm), F114P Az (red line, 600.0 nm), N47S Az (green line, 647.1 nm), and F114N Az (blue line, 647.1 nm). (B) Expanded region containing Cu−S vibrations; lines mark the positions of intensity-weighted average, $\langle\nu_{Cu-S}\rangle$, of peaks L, M, N, O. $\langle\nu_{Cu-S}\rangle$ is the same for WT and F114N Az.

to 2.211 and the magnitude of $A_{\|}$ increases from 59×10^{-4} to 68×10^{-4} cm^{-1}. The opposite behavior is observed for the N47S Az variant. Here, $g_{\|}$ increases from 2.262 to 2.283, and the magnitude of $A_{\|}$ decreases from 59×10^{-4} to 51×10^{-4} cm^{-1}. The spin Hamiltonian parameters of F114N Az are very similar to those of WT Az.

The deviation of the g value from that of the free electron (2.0023) for a Cu($3d_{x^2-y^2}$) ground state reflects the amount of copper character in the ground state and the LF excited-state energies. Ignoring ligand contributions, the deviation of the $g_{\|}$ value from 2.0023 is given by

$$g_{\|} = 2.0023 - \frac{8\lambda\alpha^2\beta^2}{E_{xy}} \quad (2)$$

where $\lambda(Cu^{2+}) = -830$ cm^{-1}, β and α are the metal $3d_{x^2-y^2}$ and $3d_{xy}$ orbital coefficients in the LF wave functions, and E_{xy} is the LF excited-state energy. With the assumption that the covalencies of the ground-state wave functions for WT Az and the variants are similar (i.e., no change in copper character), the deviation of the $g_{\|}$ value can be related to the energy of the E_{xy} LF excited state obtained from MCD data (band 7):

$$\Delta g_{\|}(\text{variant}) = \frac{E_{xy}(\text{WT})}{E_{xy}(\text{variant})}\Delta g_{\|}(WT) \quad (3)$$

Using the energies of band 7 for E_{xy}'s (from section 3.1.1) and the $g_{\|}$ value of WT Az, eq 3 predicts a $\Delta g_{\|}$ for F114P and N47S Az of 0.238 and 0.275, respectively. These predicted values deviate from the experimental $\Delta g_{\|}$ values for F114P and N47S Az of 0.211 and 0.283, respectively. Thus, eq 3 overestimates the magnitude of $\Delta g_{\|}$ for F114P Az, while it underestimates the magnitude of $\Delta g_{\|}$ for N47S Az. This discrepancy requires that the covalency of the ground-state wave function increase for F114P Az and decrease for N47S Az. The $g_{\|}$ value of F114N Az is identical to that of WT Az, indicating that there is little change in copper character between the two.

The copper hyperfine coupling is given by

$$A_{\|} = P_d((-\kappa - \frac{4}{7})\alpha^2 + \frac{3}{7}(g_{\perp} - 2.00) + (g_{\|} - 2.00)) \quad (4)$$

where $P_d = 396 \times 10^{-4}$ cm^{-1}, κ is the Fermi contact term, and α^2 is the percent metal character in the $3d_{x^2-y^2}$ orbital. Equation 4 and the experimental changes in g values allow the hyperfine coupling constants for the variants to be predicted relative to WT Az assuming no change in covalency. For F114P Az, the decrease in experimental $g_{\|}$ value accounts for a change in $A_{\|}$ from 59×10^{-4} cm^{-1} in WT Az to 78×10^{-4} cm^{-1}. (Note that $A_{\|}$ is negative.) Experimentally, however, an $A_{\|}$ of 68×10^{-4} cm^{-1} is observed. For N47S Az, the increase in $g_{\|}$ value accounts for the observed decrease in $A_{\|}$ to 51×10^{-4} cm^{-1}. The $A_{\|}$ of F114N Az is nearly identical to that of WT Az.

For F114P Az, only including the change in LF excited-state energy, E_{xy} from MCD, overestimates the change in the $g_{\|}$ value relative to WT Az. Also, the change in g value observed overestimates the change in $A_{\|}$. For N47S Az, the change in LF excited-state energy, E_{xy}, underestimates the change in the $g_{\|}$ value relative to WT Az. These data support the analysis in section 3.1.1 that, in F114P Az, removing an H-bond to the Cu^{2+}−S(Cys) bond increases the covalency of the bond. Furthermore, in N47S Az, altering the electrostatic environment near the S(Cys) ligand upon removal of the amino acid side-chain carbonyl dipole (negative side toward the S(Cys)) decreases the covalency of the Cu^{2+}−S(Cys) bond. In F114N Az, the covalency of the Cu^{2+}−S(Cys) bond does not change based on the aforementioned data.

3.1.3. Resonance Raman. The rR spectra resulting from laser excitation into band 4, the intense S(Cys)$\pi\rightarrow$ $Cu^{2+}(3d_{x^2-y^2})$ CT band, of WT Az, and the variants are presented in Figure 5 (left, 200−900 cm^{-1}; right, 330−475 cm^{-1} (normalized to peak M)). Consistent with rR data reported for other BC proteins,[75−86] the 325−475 cm^{-1} region shows several resonance-enhanced vibrational features, all of which contain some amount of Cu^{2+}−S(Cys) stretching character. The intensity-weighted average energy is generally used to determine the relative Cu^{2+}−S(Cys) bond strength:[85]

$$\left\langle \nu\text{Cu}-\text{S(Cys)} \right\rangle = \sum_i [(I_{01}^i)(\nu_i)^2] / \sum_i (I_{01}^i)(\nu_i) \quad (5)$$

Table 4 summarizes the experimentally determined $\langle\nu$Cu−S(Cys)$\rangle$ for WT Az and the variants. WT Az has a $\langle\nu$Cu−S(Cys)$\rangle$ of 407 cm^{-1}, which increases to 413 cm^{-1} for F114P Az, decreases to 402 cm^{-1} for N47S Az, and does not change for F114N Az. The higher energy region of the rR spectra (700−900 cm^{-1}) contains overtones and combination bands of the vibrational features in the 325−475 cm^{-1} region. The sharp

Table 4. $\langle\nu$Cu−S(Cys)$\rangle$ Obtained from rR

	WT Az	F114P Az	N47S Az	F114N Az
$\langle\nu$Cu−S(Cys)$\rangle$, cm^{-1}	407	413	402	407

dx.doi.org/10.1021/ja306438n | J. Am. Chem. Soc. 2012, 134, 16701−16716

feature located at ~756 cm^{-1} for WT Az has been assigned to the C_β–S(Cys) stretch. The energy of this feature remains the same in F114N Az and shifts to ~753 cm^{-1} in N47S Az. Resonance enhancement of the C_β–S(Cys) stretch is not observed for F114P Az. (The features at higher energy are too broad and located at energies that allow their assignment as overtone and combination bands). The lack of a resonance enhanced C_β–S(Cys) stretch likely results from the loss of near planarity of the Cu–S(Cys)–C_β–C_α dihedral angle for F114P Az (observed in the X-ray crystal structure, *vide infra*).

From the increase in the $\langle\nu$Cu–S(Cys)$\rangle$, removing an H-bond to the thiolate in the case of F114P Az increases the strength of the Cu^{2+}–S(Cys) bond. Conversely, for N47S Az removing a negatively oriented carbonyl dipole near the S(Cys) decreases the Cu^{2+}–S(Cys) bond strength. Replacing the phenyl with the amide dipole in the 114 position (F114N Az) does not perturb the Cu^{2+}–S(Cys) bond strength.

3.1.4. S K-Pre-edge XAS. The S K-pre-edge XAS data are shown in Figure 6. Results from fits to the pre-edge feature are given in Table 5. The pre-edge arises from the excitation of a core S 1s electron on the S(Cys) ligand into the singly unoccupied Cu($3d_{x^2-y^2}$) molecular orbital (SUMO or β-LUMO in the unrestricted formalism) (a S 1s→Cu($3d_{x^2-y^2}$) transition). The intensity of this feature is proportional to the total S_p character in the ground-state wave function (β-LUMO). Relative to WT Az, the intensity of the pre-edge increases for F114P Az, decreases for N47S Az, and exhibits little change for F114N Az. Using Pc as a reference (38 ± 3% S_p character), the intensity of the S K-pre-edge feature at ~2469 eV amounts to 45 ± 3% S_p character in the ground-state wave function of WT Az. The intensity increase of the pre-edge feature for F114P Az equates to an increase in S_p character by ~9% S_p. The decrease in pre-edge intensity for N47S Az equates to a decrease in S_p character by ~14%. F114N Az exhibits a pre-edge intensity very similar to WT Az.

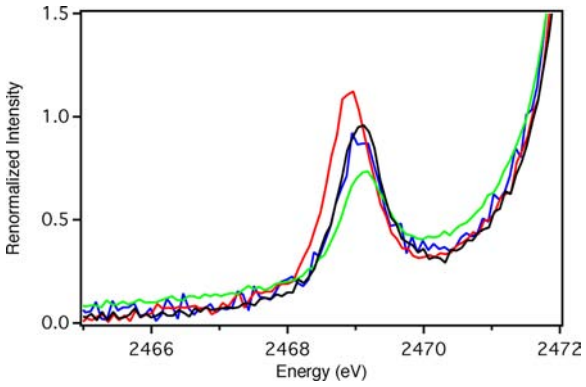

Figure 6. S K-pre-edge XAS data for WT Az (black line), F114P Az (red line), N47S Az (green line), and F114N Az (blue line). In each case, the spectra have been renormalized to account for total Cu^{2+} loading in the T1 active site.

Table 5. Results of S K-Pre-edge Fits

protein	pre-edge energy (eV)	covalency (% S_p)
WT Az	2469.1	45 ± 3
F114P Az	2468.9	54 ± 3
N47S Az	2469.1	31 ± 3
F114N Az	2469.1	43 ± 3

In summary, from sections 3.1.1–3.1.4 it is observed that removing an H-bond to the Cu–S(Cys) bond (F114P Az) increases the covalency (i.e., greater S_p character) and the Cu–S(Cys) bond strength, while for N47S Az, removing the negatively oriented carbonyl dipole near the S(Cys) decreases the covalency and the bond strength. Interestingly, for F114N Az, the spectral features are essentially identical to WT Az, with the exception that the CT absorption intensity decreases. These spectral changes allow the evaluation of electronic structure calculations, which provide insight into the contributions of the second-sphere residues to changes in covalency and electrostatics. How these each contribute to E^0 is elucidated below.

3.2. Computational. *3.2.1. Wild-Type and Perturbed Protein Sites: Calibrating Calculations to Spectroscopic Data.* As a starting point for calibrating electronic structure calculations to the spectroscopic data presented above, both **L**- and **S-WT** models have been partially geometry optimized. The relevant optimized geometric parameters are given in Table 6 and compared to an oxidized X-ray crystal structure of WT Az (PDB ID: 1JZF). The optimized Cu-ligand bond lengths of **L**- and **S-WT** are very similar to one another and consistent with experiment. These results are also in agreement with a partial geometry optimization previously reported for WT Az.[87]

The partial geometry-optimized structures of **L**- and **S-F114P** are given in Table 7. From crystallography, the F114P Az variant has a shorter Cu–S(Cys) bond than WT Az (2.21 to 2.15 Å, although the change is within the resolution of the crystallography). This change in bond length is reproduced by the partially optimized **S**- and **L-F114P** structures (2.197 to 2.176 Å for **L-WT** versus **L-F114P**; 2.205 to 2.189 Å for **S-WT** versus **S-F114P**). Besides changes in Cu–ligand bond lengths, the X-ray crystal structure of F114P Az shows a structural distortion of the S(Cys) ligand. When F114 is replaced with P114, three structural changes occur relative to WT Az: (1) the N_l–Cu–S(Cys) angle opens up from ~123° to ~139° (note the notation of N_l (or N_r) refers to the His ligand on the left (or right) side of Cu as viewed along the Cu–S(Cys) bond; see Figure 1); (2) the N_r–Cu–S–C_β dihedral angle rotates from ~−83° to ~−128°; and (3) the Cu–S–C_β–C_α dihedral rotates from ~−174° to ~−146°. These structural changes are included in **L-F114P** as this model is derived from crystallography; however, constraints on the α- and β-carbons of the S(Et) ligand in the **S-F114P** model do not allow for the rotation of the Cu–S(Cys)–C_β–C_α dihedral angle to occur. This structural change is relevant for the interpretation of the TDDFT calculations (*vide infra*).

The partial geometry-optimized structures of **L**- and **S-N47S** and **L**- and **S-F114N** are given Table 8. The DFT-derived Cu–S(Cys/Et) bond lengths of these models are similar to those of WT Az, being slightly longer for the N47S Az models. This parallels the changes in Cu–ligand bond lengths between the WT Az and the N47S/F114N Az crystal structures (Table 8).

Frequency calculations were performed on the small models in order to correlate to the $\langle\nu$Cu–S(Cys)$\rangle$ from rR spectroscopy. The calculated Cu–S(Et) stretching frequencies are given in Table 9. For **S-WT**, the calculated Cu–S(Et) frequency is 405 cm^{-1}. This value increases to 412 cm^{-1} for **S-F114P** and decreases to 402 cm^{-1} for **S-N47S**. The Cu–S(Et) frequency does not change for **S-F114N**. These calculated changes in Cu–S(Et) frequency are in agreement with the changes in $\langle\nu$Cu–S(Cys)$\rangle$ observed from rR spectroscopy.

dx.doi.org/10.1021/ja306438n | J. Am. Chem. Soc. 2012, 134, 16701–16716

Table 6. Comparison of L- and S-WT Bond Distances, Covalencies, and IEs

	oxidized			reduced		
	L-WT	**S-WT**	1JZF (1.5 Å)	**L-WT**	**S-WT**	1JZG (1.4 Å)
Cu−S(Cys)	2.197	2.205	2.21	2.281	2.288	2.23
Cu−S(Met)	3.317	3.317	3.32	3.317	3.317	3.31
Cu−N(His)$_l$	2.022	2.009	2.08	2.099	2.114	2.12
Cu−N(His)$_r$	2.066	2.038	2.02	2.173	2.130	2.06
S(Cys)−X$_l$[a]	3.526	3.439	3.44	3.502	3.439	3.44
S(Cys)−X$_r$	3.585	3.569	3.57	3.473	3.569	3.53
S(Cys)−O(CO(1))	3.576	3.431	3.48	3.459	3.414	3.52
Cu−O(CO(2))	2.548	2.597	2.60	2.554	2.597	2.67
Cu−C(CO(3))	–	–	–	–	–	–
Cu$_d$[b]	38.3	42.0	IE (eV)	4.31	4.15	
S$_p$[b]	32.5	28.7	ΔIE (eV)	–	–	
Cu$_d$[c]	43.7	46.9				
S$_p$[c]	39.2	34.0				

[a]X = N for large models and F for small models. [b]CSPA population analysis. [c]Mulliken population analysis.

Table 7. Comparison of L- and S-F114P Bond Distances, Covalencies, and IEs

	oxidized			reduced		
	L-F114P	**S-F114P**	2GHZ (1.6 Å)	**L-F114P**	**S-F114P**	2GIO (1.7 Å)
Cu−S(Cys)	2.176	2.189	2.15	2.266	2.282	2.25
Cu−S(Met)	2.847	3.317	2.92	2.847	3.317	2.71
Cu−N(His)$_l$	2.000	2.020	1.98	2.066	2.121	2.02
Cu−N(His)$_r$	2.043	2.045	2.08	2.116	2.125	2.09
S(Cys)−X$_l$[a]	–	–	–	–	–	–
S(Cys)−X$_r$	3.313	3.569	3.20	3.211	3.569	3.29
S(Cys)−O(CO(1))	3.683	3.579	3.65	3.647	3.523	3.58
Cu−O(CO(2))	3.547	2.597	3.60	3.521	2.597	3.80
Cu−C(CO(3))	–	–	–	–	–	–
Cu$_d$[b]	34.9	40.0	IE (eV)	4.23	3.97	
S$_p$[b]	35.2	34.3	ΔIE (eV)	−0.08	−0.19	
Cu$_d$[c]	40.0	44.4	ΔS$_p$[b]	2.7	5.6	
S$_p$[c]	42.9	40.5	ΔS$_p$[c]	3.7	6.5	

[a]X = N for large models and F for small models. [b]CSPA population analysis. [c]Mulliken population analysis.

Table 8. Comparison of L- and S-N47S and L- and S-F114N Bond Distances, Covalencies, and IEs

	oxidized					reduced				
	L-N47S	**S-N47S**	**L-F114N**	**S-F114N**		**L-N47S**	**S-N47S**	**L-F114N**	**S-F114N**	3JTB (1.8 Å)
Cu−S(Cys)	2.207	2.217	2.199	2.214		2.301	2.308	2.281	2.297	2.20
Cu−S(Met)	3.317	3.317	3.317	3.317		3.317	3.317	3.317	3.317	3.19
Cu−N(His)$_l$	2.019	2.002	2.026	2.017		2.098	2.113	2.113	2.132	2.26
Cu−N(His)$_r$	2.057	2.047	2.063	2.038		2.156	2.150	2.158	2.115	2.09
S(Cys)-X$_l$[a]	3.548	3.439	3.529	3.439		3.493	3.439	3.498	3.439	3.49
S(Cys)−X$_r$	3.533	3.569	3.580	3.569		3.423	3.569	3.480	3.569	3.56
S(Cys)−O(H)(CO(1))	–	–	3.574	3.430		–	–	3.465	3.407	4.13
Cu−O(CO(2))	2.578	2.597	2.549	2.597		2.558	2.597	2.549	2.597	2.82
Cu−C(CO(3))	–	–	4.586	4.672		–	–	4.586	4.650	4.88
Cu$_d$[b]	40.0	44.6	38.4	41.2	IE (eV)	4.58	4.47	4.35	4.18	
S$_p$[b]	29.5	25.6	32.4	30.3	ΔIE (eV)	0.27	0.32	0.04	0.03	
Cu$_d$[c]	46.1	49.9	43.8	45.8	ΔS$_p$[b]	−3.0	−3.1	−0.1	1.6	
S$_p$[c]	35.7	30.2	39.0	35.6	ΔS$_p$[c]	−3.5	−3.8	−0.2	1.6	

[a]X = N for large models and F for small models. [b]CSPA population analysis. [c]Mulliken population analysis.

TDDFT calculations were carried out on the small models. The calculated absorption spectra are shown in Figure 7. These generally reproduce the trends observed in experiment (i.e., little change in the energy and a decreased calculated oscillator

Table 9. Calculated Cu−S(Et) Stretching Frequencies for the Small Models

	WT Az	F114P Az	N47S Az	F114N Az
ν(Cu−S(Et)), cm^{-1}	405	412	402	405

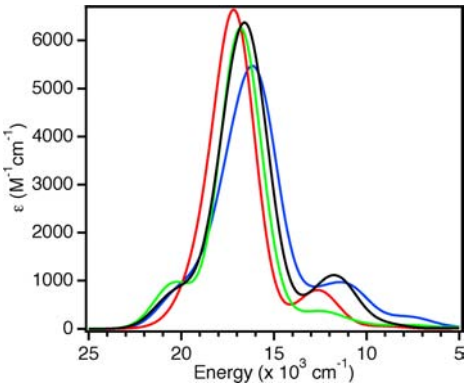

Figure 7. TDDFT calculated absorption spectra of small oxidized models **S-WT** (black line), **S-F114P** (red line), **S-N47S** (green line), and **S-F114N** (blue line).

strength (f) of the S(Cys)π→Cu($3d_{x^2-y^2}$) CT band for **S-N47S** and **S-F114N**, and a blue-shift and an increase in intensity of S(Cys)π→Cu($3d_{x^2-y^2}$) CT for **S-F114P**). The decrease in ε of band 4 in the experimental absorption spectrum of the F114N Az variant derives from a change in the donor orbital in the CT process. While the acceptor β-LUMO is the same in both **S-WT** and **S-F114N** (see below), the donor orbital changes from 38% S_p and 6% N(His) character in **S-WT** to 33% S_p and 9% N(His) character in **S-F114N**. For F114P Az, the increased ε of bands 5 and 6 observed in experiment is not reproduced by the TDDFT calculation on **S-F114P**. As noted above, however, the thiolate ligand orientation to the T1 site is modified in this variant. Extension of the TDDFT calculations to include the rotation of the N_r−Cu−S−C_β dihedral angle does reproduce the increased intensity of the LF transitions (see Supporting Information Figures S5 and S6 and associated text).

The changes in the calculated S_p character in the β-LUMO of both large and small models can be compared to the changes in S K-pre-edge intensity between WT Az and the variants. The S_p characters determined from c^2 and Mulliken population analyses are given in Tables 6−8. As observed for the preceding calculations, experimental trends are reproduced using both the large and small models. For **L-** and **S-F114P**, the calculated S_p character increases relative to **L-** and **S-WT** (Table 7). A decrease in S_p character is calculated for the **L-** and **S-N47S** models (Table 8). Both **L-** and **S-F114N** have very limited change in S_p character relative to **L-** and **S-WT** models (Table 8).

In order to calculate the adiabatic IEs, the reduced geometries of the large and small models have been optimized in the same way as outlined above for the oxidized sites (section 2.6). Relevant structural information is given in Tables 6−8. For comparison to known structural data, only reduced X-ray crystal structures exist for WT Az and F114P Az; for both, the changes in Cu−ligand bond lengths between the oxidized and reduced X-ray crystal structures are within the resolution. Likewise, for all DFT partially geometry optimized models here only small changes in the Cu−S(Cys/Et) and Cu−N(His) bond lengths were observed (~0.1 Å increase upon reduction). The adiabatic IEs can be calculated by taking the difference in energy between the optimized oxidized and reduced structures (Tables 6−8). These values can be compared to changes in E^0 in Table 1. The IEs for the **L-** and **S-WT** models are calculated to be 4.31 and 4.15 eV, respectively. These values serve as reference points for the variant models. The calculated changes in IE for the **L-** and **S-F114P** models (relative to **L-** and **S-WT**) are −80 and −190 mV, respectively. The IEs of **L-** and **S-N47S** both increase by 270 and 320 mV, respectively. Similarly, more positive IEs were calculated for **L-** and **S-F114N** (40 and 30 mV, respectively). The calculated IEs for the variants relative to WT Az follow the same trends as the experimental changes in E^0 (Table 1).

Throughout this Section, we have found that there is a good correlation between the calculated and observed spectroscopic data and for trends in E^0. It is also interesting to note that, in the case of F114N Az, there are little spectral changes despite a change in E^0 in both experiment and calculation. We proceed to systematically investigate the effects of H-bonding and carbonyl dipoles on the BC active site and evaluate their contributions to changes in E^0.

3.2.2. Modeling Hydrogen Bonds. While H-bonding to the Cu−S bond in BC has been considered to some extent computationally,[28] it is first important to note that the ground-state wave function of the T1 site is highly covalent and anisotropic along the thiolate(π)−Cu^{2+} bond (Figure 8, left). The relative H-bonding interaction with the S(Et) is therefore dependent on the orientation of the H-bond donor to the β-LUMO. This orientation is characterized by two angles (Figure 8, right): (1) the Cu−S(Et)−H(δ^+) angle φ (where δ^+ represents the partial positive charge of the H-bond donor), and (2) the S(Met)−Cu−S(Et)−H(δ^+) dihedral angle θ. Two limits have been considered; these are termed active and passive H-bonding.[88] The active orientation for H-bonding is defined as having a Cu−S(Et)−H(δ^+) angle of 90° and a S(Met)−Cu−S(Et)−H(δ^+) dihedral angle of ~90° (i.e., the H(δ^+)−X(δ^-) unit is in the plane of the Cu−S π-bond). The passive orientation also has a Cu−S(Et)−H(δ^+) angle of 90°, but the S(Met)−Cu−S(Et)−H(δ^+) dihedral angle is rotated to 180° (i.e., perpendicular to the S π-bond). The calculated

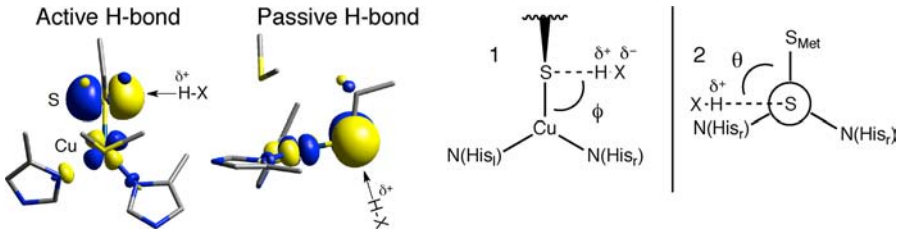

Figure 8. (Left) Active and (middle) passive orientations for H-bonding to the Cu−S(Cys) bond. (Right) 1, Cu−S(Cys)−H bond angle; 2, S(Met)−Cu−S(Cys)−H bond dihedral angle (Newman projection along Cu−S(Cys) bond).

dx.doi.org/10.1021/ja306438n | J. Am. Chem. Soc. 2012, 134, 16701−16716

covalency and IE for the active and passive orientations as a function of H-bond (H−F as the H-bond donor) distance from the S of the Cu−S(Et) bond are given in Figure 9 and tabulated in Supporting Information Tables S1−S3.

For both active (black circles) and passive (red circles) orientations the calculated IE of the reduced site increases as the H-bond distance decreases (Figure 9A; relative to an H-bond at 10 Å). However, as the S···F distance decreases, the IE increases more sharply for the active orientation than the passive. At 3.5 Å (similar to the crystallographic N−S distance for H-bonds to S(Cys) residues in BC proteins) the ΔΔIE between the active and passive orientations is ∼90 mV.

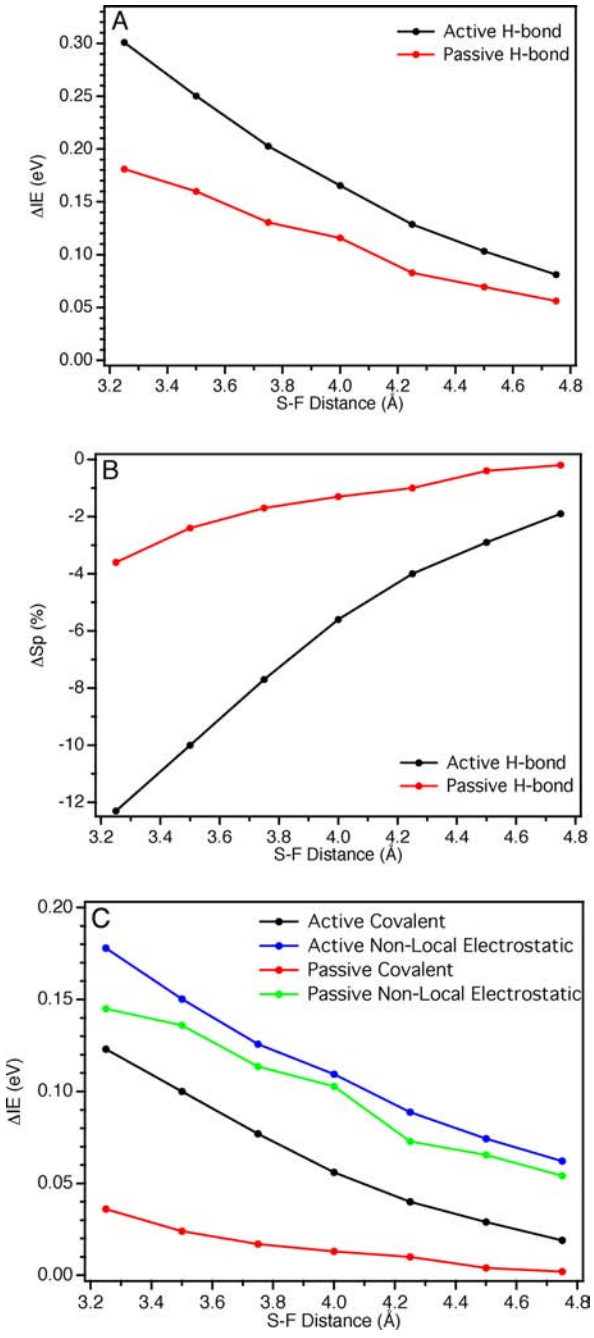

Figure 9. (A) Dependence on the calculated IE of the reduced model. (B) Dependence on the calculated S_p character in the β-LUMO of the oxidized model on the orientation (active versus passive) and distance of an H-bond from the Cu−S(Cys) bond. (C) Covalent and nonlocal electrostatic components to the IE for both active and passive orientations.

The change in the calculated S_p character in the β-LUMO as a function of H-bond distance is also orientation dependent (Figure 9B). A decrease in the H-bond distance leads to a significantly larger decrease in the S_p character in the β-LUMO for the active H-bond orientation relative to the passive orientation. At 3.5 Å, this difference is 7.6% S_p. Note that there is very little change in covalency for the passive H-bond orientation. We also note that the calculated difference in S_p character between active and passive orientations (7.6%) is not sensitive to PCM solvation (despite the Cu−S(Cys) bond itself being quite sensitive, see Supporting Information Table S9 and associated text),[36,89] consistent with the H-bonding interaction being mostly ionic in nature.[38,88,90−93] Therefore, the difference in the calculated IE between the active and passive orientations can be ascribed to the difference in Cu−S(Et) covalency. Importantly, this allows the total change in the IE of the reduced site to be fractioned into an electrostatic component and a covalent component. The electrostatic component is referred to as nonlocal electrostatics. *Thus, the relative contributions of the nonlocal electrostatic and covalent components to the IE can be quantified* (Figure 9C; also given in Table S3). At 3.5 Å, the IE and S_p character between active and passive orientations differ by 90 mV and 7.6% S_p, respectively. An estimate of the covalent component is thus ∼−12 mV/% S_p. The negative slope of this correlation indicates that, as the covalency of the Cu−S(Et) bond increases, the IE decreases and thus E^0 decreases. For comparison, a Mulliken population analysis gives a $\Delta\Delta S_p$ of 9.7% S_p, which results in a slope of ∼−9 mV/% S_p. Therefore, this model predicts a slope for the covalent contribution to the IE of −10 ± 2 mV/% S_p. Importantly, from this analysis, an active H-bond to a S−M^{n+} bond in an ET protein will have both a nonlocal electrostatic and a covalent component to E^0; these contributions to E^0 are additive and comparable in magnitude.

3.2.3. Modeling Carbonyl Dipoles. In this Section we investigate the distance and orientation dependence (relative to the Cu−S(Et) bond) of carbonyl dipoles on the calculated IE and S_p character. In particular, we evaluate the relative contribution of changes in covalency and nonlocal electrostatics to the IE.

Five dipole orientations relative to the Cu−S(Et) bond have been investigated (Figure 10C). The distance for each orientation is measured from the dipole to (1) and (2) the Cu; (3) the midpoint of the Cu−S(Et) bond; and (4) and (5) the S (see Supporting Information Figure S4 for geometric parameters for each dipole orientation). The distance dependencies on the calculated ΔIE and ΔS_p character for these dipole orientations are given in Figure 10A and B, respectively (ΔIE and ΔS_p are relative to the calculated value with a dipole at 10 Å). The results of these calculations are also summarized in Supporting Information Tables S4−S8. For all orientations considered, when the dipole is brought closer to the T1 site on either the Cu or S side of the Cu−S(Et) bond with the negative side of the dipole oriented toward the bond, the calculated ΔIE decreases systematically (Figure 10A). This decrease in IE reflects the electrostatic destabilization of the electron in the RAMO, which lowers E^0. The result obtained here is consistent with experiment (i.e., the N47S Az variant eliminates a dipole that is negatively oriented toward the S side of the Cu−S(Cys) bond and has a higher E^0 than WT Az (Table 1)) and previous calculations.[28] The ΔIEs for orientations 1−5 at a distance of

dx.doi.org/10.1021/ja306438n | J. Am. Chem. Soc. 2012, 134, 16701−16716

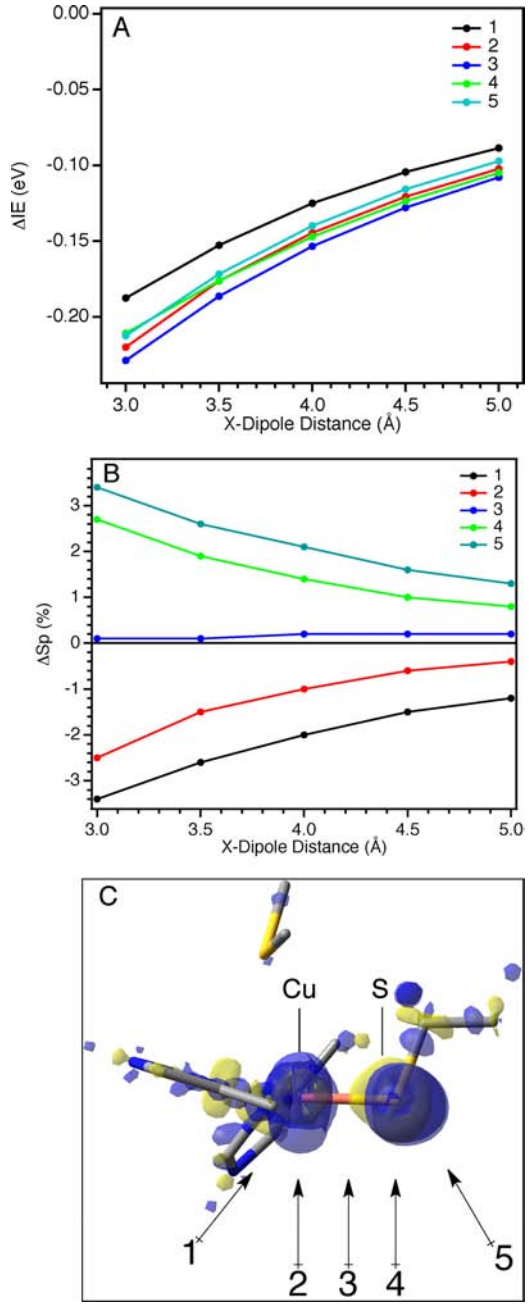

Figure 10. (A) Dependence on the calculated IE of the reduced model for different dipole orientations and distances. (B) Dependence on the calculated S_p character in the β-LUMO of the oxidized model. (C) Orientations (1−5) of dipoles from the Cu−S(Cys) bond considered in the text.

3.5 Å are −153, −176, −186, −176, and −172 mV, respectively (Table 10). However, it is important to note that, as determined from the analysis in section 3.2.2, there can be a significant covalent component as well as a nonlocal electrostatic contribution to these changes in IE. From Figure 10B, both the magnitude and the sign of the calculated ΔS_p character changes depending on the dipole's orientation relative to the Cu−S(Et) bond. Bringing a negatively oriented dipole close the Cu side of the Cu−S(Et) bond (orientations 1 and 2) decreases the S_p character in the β-LUMO. Conversely, bringing the dipole toward the S side of the Cu−S(Et) bond (orientations 4 and 5) increases the S_p character. Interestingly, when the dipole

Table 10. Calculated ΔIE, ΔS_p Character, and Covalency Corrected ΔIE for Dipoles in Orietations 1−5 at a Distance of 3.5 Å from the Cu−S(Et) Bond

orientation	ΔIE (mV)	ΔS_p (%)	cov. IE corr. (mV)	ΔIE corr. (mV)
1	−153	−2.6	26	−179
2	−176	−1.5	15	−191
3	−186	0.1	−1	−185
4	−176	1.9	−19	−157
5	−172	2.6	−26	−146

is in orientation 3 (i.e., oriented at the midpoint of the Cu−S(Et) bond), the S_p character does not change with distance (Figure 10B, blue circles). Therefore, the calculated ΔIEs in Figure 10A contain covalent contributions that differ in sign and magnitude depending on the dipole orientation being considered. Taking the covalent contribution to be −10 ± 2 mV/% S_p (from section 3.2.2), the calculated ΔIE's can be corrected for these differences in covalency (Tables S4−S8). For orientations 1−5 and at a distance of 3.5 Å from the Cu−S(Et) bond, the covalency corrected ΔIE's are −179, −191, −185, −157, and −146 mV, respectively (Table 10), which represent the nonlocal electrostatic contribution to the IE of the T1 site due to the presence of the dipole in the orientations given in Figure 10C. The magnitudes follow the order 2 > 3 > 1 > 4 > 5, which reflects the energetics of the interaction of the dipole with the electron charge distributed over the Cu−S(Et) bond. To consider the energetics in more detail, the negative charge distribution can be estimated from the electron density difference between the reduced and oxidized T1 site (Figure 10C; blue and yellow regions represent the differences in negative and positive charge, respectively). A large fraction of the negative charge density is located on the Cu, but is partially delocalized onto the S. Note that the charge on the Cu extends into the region below the plane due to the asymmetric ligand distribution. The potential energy of interaction between the negatively oriented dipole and the negative charge density is inversely dependent on the square of the distance and the cosine of the angle between the dipole and the negative charge. This consideration reproduces the calculated trend (i.e., 2 > 3 > 1 > 4 > 5). It is interesting to compare the total calculated ΔIE's to the covalent corrected values (Table 10). The relative magnitudes of the total ΔIE's calculated for dipoles oriented near the S side of the Cu−S(Et) bond (orientations 4 and 5) are increased due to the covalent component while those on the Cu side (orientations 1 and 2) are decreased.

In summary, from this analysis, a negatively oriented dipole has for all orientations a nonlocal electrostatic component that lowers the IE and E^0. However, if the negatively oriented dipole is on the Cu side of the Cu−S bond, the covalency of the bond decreases while if the dipole is on the S side of the Cu−S bond, the covalency increases. Thus, *the change in Cu−S covalency can either add to or oppose the change in the IE energy due to nonlocal electrostatics*. When the direction of the dipole is inverted (i.e., positive side toward the Cu−S(Et) bond), a parallel behavior as described above is obtained but with the opposite sign (see Tables S4−S8). The origin of the difference in S_p character for dipoles oriented toward either the Cu or S side of the Cu−S bond is addressed in the Discussion.

Finally, this analysis can be applied to the N47S and F114N Az variants. When a dipole located at the crystallographic position of N47 (see Figure 2) is removed, the calculated IE increases by ∼470 mV, and the S_p character decreases by 8.4%

dx.doi.org/10.1021/ja306438n | J. Am. Chem. Soc. 2012, 134, 16701−16716

S_p. The decrease in covalency contributes additively to the increase in IE. The covalent component can be subtracted to obtain the nonlocal electrostatic contribution to the IE (~385 mV). Furthermore, when a dipole is inserted at the crystallographic position of N114 (see Figure 2), the IE increases by ~210 mV with little change in S_p character (0.4% S_p).

4. DISCUSSION

A large range of reduction potentials has been measured for a series of second-sphere variants of Az, including F114P, N47S, and F114N Az.[27] In this study, a combination of spectroscopic methods has found changes in the covalencies and strengths of the Cu−S(Cys) bonds in F114P and N47S Az, where an H-bond to S has been eliminated and a negatively facing carbonyl dipole near S was deleted, respectively. Interestingly, in the case of the F114N Az variant, where a positively facing dipole is inserted ~5 Å from the Cu, a change in E^0 is observed without an associated change in the Cu−S(Cys) covalency and bond strength. This led to the development a method to fractionate the change in E^0 due to second-sphere effects into covalent and nonlocal electrostatic components. Specifically, the covalent contribution to the IE of the BC site is obtained experimentally from S K-edge XAS and estimated using a computational model involving active and passive H-bonding. In the active H-bond orientation (i.e., oriented along the RAMO in Figure 1), the covalency of the Cu−S(Cys) bond decreased, while in the passive case, the H-bond (at the same distance and angle as in the active case) affected the covalency to a lesser extent. These results allowed for the definition and quantification of the covalent (~−10 mV/% S_p) and nonlocal electrostatic contributions to the IE and thus E^0. The nonlocal electrostatic contribution is defined as the interaction energy between an electron distributed across the molecular orbital from which it is ionized and the partial charges and dipoles of the protein environment. The covalent component reflects the modulation of the ligand−metal bond due to a local second-sphere effect, which changes the nature of the molecular orbital from which the electron is ionized. The more covalent the ligand−metal bond, the greater the stabilization of the oxidized state over the reduced state (decreasing E^0). This relates to the greater antibonding character of the RAMO, which decreases the IE and thus E^0. The nonlocal electrostatic term has been well modeled for ET proteins using QM/MM calculations,[30,33,37,51,94] with some of these calculations including a contribution from the polarization of the solute by the protein and solvent.[51,95,96] The solute polarization is related to the covalent component. However, the method employed here has the advantage of a direct estimation of each contribution separately as the difference in S covalency is experimentally determined by the S K-edge XAS data.

A comparison of the results for BC presented here with these for FeS clusters is insightful. For FeS clusters, a correlation of E^0 with % S_p change in covalency (per Fe) was ~−8 mV/% S_p.[38,39] Also, in a series of P450 model complexes, addition of two H-bonds to the Fe−SPh bond increased E^0 by ~330 mV and decreased the covalency by ~19% S_p.[90] From the analysis here, the change in E^0 due to H-bonding has both a nonlocal electrostatic as well as a covalent contribution. Using the covalent component of ~−8 mV/% S_p from the FeS clusters, the nonlocal electrostatic contribution associated with two H-bonds to the thiolate is ~180 mV (the covalent component being ~150 mV), which is similar to the nonlocal electrostatic component obtained here for BC. Therefore, a reasonable estimate for the nonlocal electrostatic component to E^0 is ~100 mV/H-bond. It should be noted that the slope estimated for the covalent contribution for the Cu−S(Cys) bond in the T1 site (~−10 mV/% S_p) need not be the same for other sulfur−metal bonds.

Previous observations of a linear dependence of E^0 on covalency was understood using a valence bond configuration interaction (VBCI) model.[90] This VBCI model can be extended to gain insight into the origin of the covalency change and its contribution to E^0 due to changes in the electrostatic environment around the BC site. If a positive charge (or positively oriented dipole as in the case of H-bonding) is located near the thiolate ligand, it will interact energetically with the ligand-based S(3p) valence orbitals. Of particular importance is the out-of-plane S(3p) orbital, which is π antibonding to the Cu($3d_{x^2-y^2}$) orbital in the SOMO. The energy stabilization of this orbital, defined here as δ, due to a charge or dipole can be thought of in terms of the electrostatic stabilization energy of an electron in the ligand-based S(3p) orbital. δ is negative for attractive and positive for repulsive interactions. The crystal field Hamiltonian for an electron in a p orbital in the presence of one positive charge is

$$H_{xf} = -\frac{Ze^2}{a} - \frac{Ze^2}{2a^3}(3z^2 - r^2) \quad (6)$$

where Z if the effective nuclear charge, e is an electron charge, and a is the distance between the ligand and the positive charge. The contribution to δ for active and passive orientations can be obtained by evaluating H_{xf} on either a $3p_z$ or a $3p_{x,y}$ atomic orbital, respectively (Figure 11). This gives the

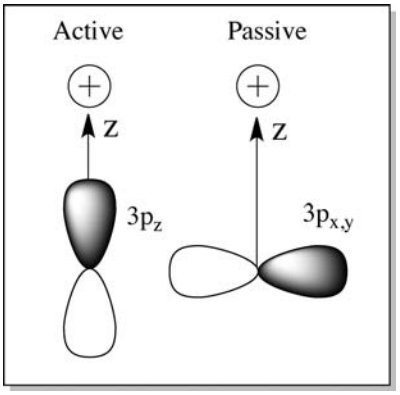

Figure 11. Crystal field model for point charges near the thiolate ligand-based S_{3p} orbitals.

following expressions: $-(Ze^2/a) - (2Ze^2/5a^3)\langle r_{3p}{}^2\rangle$ (active) and $-(Ze^2/a) + (Ze^2/5a^3)\langle r_{3p}{}^2\rangle$ (passive). $\langle r_{3p}{}^2\rangle$ is the average distance squared of an electron in a 3p atomic orbital from the nucleus. The values of the two terms were evaluated using DFT calculations.[97] The first term is approximately three times the value of the second, and the second further stabilizes the electron in the active orientation but destabilizes it in the passive orientation, which results in estimations of $\delta = -0.30$ eV (active) and −0.15 eV (passive). δ can be incorporated into the VBCI model (Figure 12) to increase the energy separation (Δ) between the Cu(3d) and S(3p) orbitals before bonding. The amount of ligand character in the ground-state wave function, $c_L{}^2$ (measured by the S K-edge XAS data), is $(H_{ML})^2/\Delta^2$, where H_{ML} is the resonance integral reflecting ligand−metal overlap. When $\delta < \Delta$, which should be the case for H-bonding

dx.doi.org/10.1021/ja306438n | J. Am. Chem. Soc. 2012, 134, 16701−16716

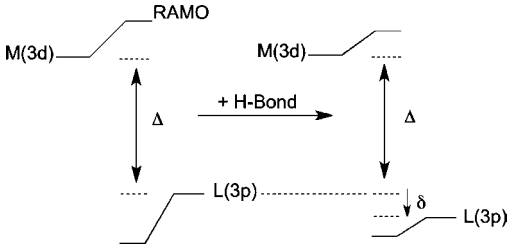

Figure 12. VBCI model illustrating the effect of H-bonding and δ on the ligand−metal bonding.

to a ligand−metal bond, the change in c_L^2 upon H-bonding will vary linearly with δ (see Supporting Information). Specifically, a more negative value of δ (greater stabilization energy) will decrease c_L^2. Furthermore, the change in δ can be correlated to the change in reduction potential (see Supporting Information). For $\delta < \Delta$, ΔE_{redox} increases linearly with increase in the magnitude of δ (more negative) as this leads to less antibonding character in the RAMO. Thus, the electrostatic interaction with the S($3p_z$) orbital in Figure 11 stabilizes (or destabilizes if repulsive) the ligand-based orbital in energy by δ, which decreases c_L^2 and increases E^0. Finally, we note that this VBCI approach can be related to the empirical valence bond model of Warshel,[98,99] where the environment interacts with the ionic character of the ground-state wave function. This will be larger for the reduced than the oxidized state due to the larger covalency of the BC RAMO in Figure 1, therefore affecting the energy more for the reduced site. Here, we use the effect of the environment on the covalency of the oxidized site to evaluate this contribution to E^0.

Secondary structural and electronic changes can occur due to point mutations. These can lead to changes in E^0 either through covalent or nonlocal electrostatic contributions. This is important to consider for the variants studied here and in general. DFT calculations (*vide supra*, section 3.2.2) predicted an ∼250 mV increase in the IE of the T1 site due to an active H-bond. This change in IE resulted from both the decrease in covalency (due to a stabilization of the S($3p_z$) orbital by δ in Figure 12) as well as the nonlocal electrostatic term—both of these contributions being additive in increasing E^0. In the F114P Az variant, a single active H-bond to the Cu−S(Cys) bond has been removed. However, the E^0 of the F114P Az variant only decreases by ∼95 mV relative to WT Az. The spectroscopic data indicate that there is an increase in the covalency as well a strengthening of the Cu−S(Cys) bond in F114P Az. The increase in covalency by ∼9% S_p accounts for an ∼90 mV decrease in E^0. This suggests that the remaining nonlocal electrostatic component to E^0 from the H-bond has decreased or been compensated. Insight into this decrease/compensation can be obtained by comparing the X-ray crystal structure of F114P Az to that of WT Az. In WT Az, the phenyl ring of F114 shields the T1 active site from H_2O. As has been observed previously,[41] substituting this residue with Pro in the F114P Az variant opens a H_2O accessible pocket near the T1 site. This allows access of four water molecules (present in both oxidized and reduced crystal structures of F114P Az). One of these water molecules is present with a H_2O−O(C) distance of ∼2.9 Å from the *trans*-axial carbonyl ligand of the T1 site. The Cu−O(C) distance has also increased from ∼2.6 Å in WT Az to ∼3.6 Å in F114P Az.[41] DFT calculations indicate that considering just the one water dipole and the increase in carbonyl−Cu distance increases the IE of the T1 site by ∼50 mV with little change in covalency. Thus, the increased solvation (four H_2Os) adds an additional electrostatic term that opposes the nonlocal electrostatic change in E^0 associated with the removal of the H-bond to the Cu−S(Cys) bond. There can also be contributions to E^0 from changes in the LF environment of F114P Az, but these are expected to be small relative to the other perturbations considered here.

The F114N and the N47S Az variants involve the insertion and deletion of a carbonyl dipole, respectively. In section 3.2.3, DFT calculations determined that a dipole in the vicinity of the T1 site could significantly alter the IE through both changes in covalency and nonlocal electrostatics. The change in covalency due to the presence of the dipole could be either additive to or oppose the nonlocal electrostatic effect on the IE depending on the orientation of the dipole relative to the Cu−S(Cys) bond. With a negatively facing dipole on the S side of the Cu−S(Cys) bond, δ in Figure 12 is positive. This increases the covalency, which further decreases the IE (in parallel with the nonlocal electrostatics). However, with a negative dipole on the Cu side of the Cu−S(Cys) bond, the energy of the Cu(3d) orbital in Figure 12 increases; thus Δ increases and the covalency decreases, which opposes the nonlocal electrostatic decrease in IE due to the presence of the negative dipole. These results can be used to understand the experimental observations for the F114N and N47S Az variants, which both have an increased E^0 by ∼130 mV relative to WT Az. For F114N Az, DFT calculations reproduce the observation of a change in E^0 with little change in covalency (ΔIE ≈ 210 mV and Δ% S_p = 0.4) (section 3.2.3). This suggests that the experimentally observed change in E^0 for F114N Az is solely accounted for by the nonlocal electrostatic contribution to the IE due to the presence of the dipole. The lack of a significant change in covalency for this variant reflects its ∼5 Å distance from Cu (see Figure 2) as the covalent contribution to the IE falls off more rapidly with distance than the nonlocal electrostatic term (see Figure 9C). The increase in E^0 by ∼130 mV for N47S Az can be accounted for by the decrease in covalency of the Cu−S(Cys) bond. The experimental decrease in S_p character is ∼14% S_p, which equates to an ∼140 mV increase in E^0. DFT calculations that involve the removal of the dipole from the N47 position resulted in a decrease in covalency by 8.4% S_p and an increase in the IE by ∼470 mV. Subtraction of the covalent contribution to the IE resulted in a nonlocal electrostatic component of ∼380 mV. This suggests that there is a significant compensation of the nonlocal electrostatic component. Comparison of crystal structures containing the N47S mutation (i.e., N47S/M121L Az and N47S/F114N Az) with WT Az indicates that this mutation does not result in significant alteration of the secondary protein structure or solvent access near the T1 site. However, the N47 residue is involved in an H-bond network between two T1 ligand-containing loops. BC variants in which this residue is mutated have been found to undergo a large change in the entropic component to E^0 due to the modification of this H-bond network.[48] The final results for E^0 tuning in the Az variants relative to WT Az are summarized in Figure 13. It is observed that the covalent contribution is well estimated from S K-edge XAS, which, when combined with the total change in E^0, allows the nonlocal electrostatic contribution to be estimated experimentally. It is further observed that mutations can produce additional changes in the protein environment that can significantly impact the nonlocal electrostatic component relative to that expected based solely on the point mutation.

dx.doi.org/10.1021/ja306438n | J. Am. Chem. Soc. 2012, 134, 16701−16716

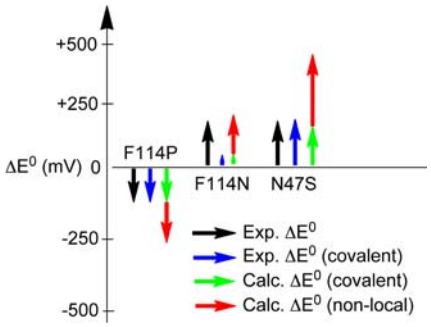

Figure 13. Illustration of the experimentally derived covalent and nonlocal electrostatic contributions to E^0 for the variants of Az relative to WT Az and their comparison to calculations.

It is interesting to extend the concepts developed here to other redox-active metalloproteins involved in ET and catalysis. In ET proteins, outer-sphere interactions have been demonstrated to strongly modulate reduction potentials and ET flow, while for enzymes they can direct reactivity.[100] The methodology given here is capable of dissecting second-sphere interactions into local covalent and nonlocal electrostatic components. In particular, for two redox active metal ions in proteins that have identical first coordination spheres but very different E^0's, the difference in E^0 due to variations in ligand–metal covalency can be defined experimentally by S K-edge XAS. This is a strong point of emphasis and a powerful tool due to the highly covalent nature of ET active sites in biology. The remaining difference in E^0 can then be attributed to variations in nonlocal electrostatics. The covalent component will be dominated by second-sphere interactions within ∼5 Å of the active site; these local interactions include active H-bonds and carbonyl dipoles with specific orientations to the ligand–metal bond. (We note that the sum of the charges and dipoles of the protein and solvent at distances of >5 Å can also contribute to the covalent component, however this is likely small relative to the local contributions.) When the experimental data (i.e., covalent and nonlocal electrostatics) are combined with structural differences from X-ray crystallography, the origin(s) of the shift in E^0 between the two active sites can be rigorously defined. This effectively uncouples specific local interactions from more long-range protein/active site interactions—a major goal in understanding outer-sphere effects in ET and catalysis. Indeed, using S K-edge XAS, we have already observed protein[39,40] and solvent[38] effects on the covalency of Fe–S bonds in the FeS ET proteins and in the heme and non-heme iron enzymes P450[92] and superoxide reductase (SOR),[91] respectively, that tune redox processes in the former and O_2 and O_2^- activation in the latter. A full understanding of these effects now allows their further extension to other systems, be they biological or synthetic.

5. SUMMARY

This study shows that in a series of second-sphere variants of the T1 site in Az, the changes in E^0 can be decomposed into a covalent and a nonlocal electrostatic component; the covalent component is directly estimated from the experimental S K-edge XAS data. When the change in E^0 due to a change in covalency of the active site is accounted for, the remaining difference in the enthalpic contribution to E^0 can be attributed to changes in the nonlocal electrostatic contribution, thus uncoupling the two terms. Both the covalent and nonlocal electrostatic contributions can be significant, comparable in magnitude, and additive for active H-bonds, and can be additive or oppose one another for dipoles. The nonlocal electrostatic term for dipoles is dependent on the distance and angle between the dipole and the charge distribution of the electron being ionized. Furthermore, for point mutations where an H-bond or charge/dipole is added or substituted, additional changes in the vicinity of the active site occur, which can partially compensate the nonlocal electrostatic effects of the mutation. For BC sites with equivalent first coordination spheres but E^0's that vary by >400 mV, as in the T1 centers in the MCOs, this large range of tunability reflects the high covalency and polarizability of the Cu^{2+}–S(Cys) bond of the T1 site and its response to the protein environment.

■ ASSOCIATED CONTENT

Supporting Information

Full ref 58; Gaussian resolution of absorption and MCD data; Cartesian coordinates of the **L** and **S** DFT structures discussed in the manuscript; supplementary figures and text including the VBCI model. This material is available free of charge via the Internet at http://pubs.acs.org.

■ AUTHOR INFORMATION

Corresponding Author

edward.solomon@stanford.edu

Notes

The authors declare no competing financial interest.

■ ACKNOWLEDGMENTS

This work was supported by grants NSF CHE-0948211 (E.I.S.), NIH DK-31450 (E.I.S.), NIH RR-001209 (K.O.H.), NSF CHE-1058959 (Y.L). The SSRL Structural Molecular Biology program is supported by the Department of Energy, Office of Biological and Environmental Research, and by the National Institutes of Health, National Institute of General Medical Sciences (including P41GM103393), and the National Center for Research Resources (P41RR001209). R.G.H. acknowledges a Gerhard Casper Stanford Graduate Fellowship. We thank Yang Ha for help analyzing the S K-edge XAS data.

■ REFERENCES

(1) Malkin, R.; Malmström, B. G. *Adv. Enzymol. Relat. Areas Mol. Biol.* **1970**, *33*, 177.
(2) Adman, E. T. *Adv. Protein Chem.* **1991**, *42*, 145.
(3) Gray, H. B. *Chem. Soc. Rev.* **1986**, *15*, 17.
(4) Holm, R. H.; Kennepohl, P.; Solomon, E. I. *Chem. Rev.* **1996**, *96*, 2239.
(5) Crane, B. R.; Di Bilio, A. J.; Winkler, J. R.; Gray, H. B. *J. Am. Chem. Soc.* **2001**, *123*, 11623.
(6) Colman, P. M.; Freeman, H. C.; Guss, J. M.; Murata, M.; Norris, V. A.; Ramshaw, J. A. M.; Venkatappa, M. P. *Nature (London)* **1978**, *272*, 319.
(7) Guss, J. M.; Freeman, H. C. *J. Mol. Biol.* **1983**, *169*, 521.
(8) Guss, J. M.; Bartunik, H. D.; Freeman, H. C. *Acta Crystallogr., Sect. B: Struct. Sci.* **1992**, *B48*, 790.
(9) Nar, H.; Messerschmidt, A.; Huber, R.; Van de Kamp, M.; Canters, G. W. *J. Mol. Biol.* **1991**, *221*, 765.
(10) Hart, P. J.; Nersissian, A. M.; Herrmann, R. G.; Nalbandyan, R. M.; Valentine, J. S.; Eisenberg, D. *Protein Sci.* **1996**, *5*, 2175.
(11) Germann, U. A.; Muller, G.; Hunziker, P. E.; Lerch, K. *J. Biol. Chem.* **1988**, *263*, 885.
(12) Messerschmidt, A.; Huber, R. *Eur. J. Biochem.* **1990**, *187*, 341.

(13) Lowery, M. D.; Solomon, E. I. *Inorg. Chim. Acta* **1992**, *198*−*200*, 233.
(14) Solomon, E. I. *Inorg. Chem.* **2006**, *45*, 8012.
(15) Solomon, E. I.; Szilagyi, R. K.; DeBeer George, S.; Basumallick, L. *Chem. Rev.* **2004**, *104*, 419.
(16) Solomon, E. I.; Hadt, R. G. *Coord. Chem. Rev.* **2011**, *255*, 774.
(17) Gewirth, A. A.; Solomon, E. I. *J. Am. Chem. Soc.* **1988**, *110*, 3811.
(18) Penfield, K. W.; Gay, R. R.; Himmelwright, R. S.; Eickman, N. C.; Norris, V. A.; Freeman, H. C.; Solomon, E. I. *J. Am. Chem. Soc.* **1981**, *103*, 4382.
(19) Shadle, S. E.; Penner-Hahn, J. E.; Schugar, H. J.; Hedman, B.; Hodgson, K. O.; Solomon, E. I. *J. Am. Chem. Soc.* **1993**, *115*, 767.
(20) Berry, S. M.; Ralle, M.; Low, D. W.; Blackburn, N. J.; Lu, Y. *J. Am. Chem. Soc.* **2003**, *125*, 8760.
(21) Garner, D. K.; Vaughan, M. D.; Hwang, H. J.; Savelieff, M. G.; Berry, S. M.; Honek, J. F.; Lu, Y. *J. Am. Chem. Soc.* **2006**, *128*, 15608.
(22) DeBeer George, S.; Basumallick, L.; Szilagyi, R. K.; Randall, D. W.; Hill, M. G.; Nersissian, A. M.; Valentine, J. S.; Hedman, B.; Hodgson, K. O.; Solomon, E. I. *J. Am. Chem. Soc.* **2003**, *125*, 11314.
(23) Ghosh, S.; Xie, X.; Dey, A.; Sun, Y.; Scholes, C. P.; Solomon, E. I. *Proc. Natl. Acad. Sci. U.S.A.* **2009**, *106*, 4969.
(24) Malmström, B. G. *Eur. J. Biochem.* **1994**, *223*, 711.
(25) Williams, R. J. P. *Eur. J. Biochem.* **1995**, *234*, 363.
(26) Gray, H. B.; Malmström, B. G.; Williams, R. J. P. *J. Biol. Inorg. Chem.* **2000**, *5*, 551.
(27) Marshall, N. M.; Garner, D. K.; Wilson, T. D.; Gao, Y.-G.; Robinson, H.; Nilges, M. J.; Lu, Y. *Nature* **2009**, *462*, 113.
(28) Li, H.; Webb, S. P.; Ivanic, J.; Jensen, J. H. *J. Am. Chem. Soc.* **2004**, *126*, 8010.
(29) Cascella, M.; Magistrato, A.; Tavernelli, I.; Carloni, P.; Rothlisberger, U. *Proc. Natl. Acad. Sci. U.S.A.* **2006**, *103*, 19641.
(30) Olsson, M. H. M.; Hong, G.; Warshel, A. *J. Am. Chem. Soc.* **2003**, *125*, 5025.
(31) Botuyan, M. V.; Toy-Palmer, A.; Chung, J.; Blake, Ii, R. C.; Beroza, P.; Case, D. A.; Dyson, H. J. *J. Mol. Biol.* **1996**, *263*, 752.
(32) Berry, S. M.; Baker, M. H.; Reardon, N. J. *J. Inorg. Biochem.* **2010**, *104*, 1071.
(33) Hong, G.; Ivnitski, D. M.; Johnson, G. R.; Atanassov, P.; Pachter, R. *J. Am. Chem. Soc.* **2011**, *133*, 4802.
(34) Si, D.; Li, H. *J. Phys. Chem. A* **2009**, *113*, 12979.
(35) Churg, A. K.; Warshel, A. *Biochemistry* **1986**, *25*, 1675.
(36) Warshel, A.; Papazyan, A. *Proc. Natl. Acad. Sci. U.S.A.* **1996**, *93*, 13665.
(37) Stephens, P. J.; Jollie, D. R.; Warshel, A. *Chem. Rev.* **1996**, *96*, 2491.
(38) Dey, A.; Jenney, F. E., Jr.; Adams, M. W. W.; Babini, E.; Takahashi, Y.; Fukuyama, K.; Hodgson, K. O.; Hedman, B.; Solomon, E. I. *Science* **2007**, *318*, 1464.
(39) Anxolabehere-Mallart, E.; Glaser, T.; Frank, P.; Aliverti, A.; Zanetti, G.; Hedman, B.; Hodgson, K. O.; Solomon, E. I. *J. Am. Chem. Soc.* **2001**, *123*, 5444.
(40) Glaser, T.; Bertini, I.; Moura, J. J. G.; Hedman, B.; Hodgson, K. O.; Solomon, E. I. *J. Am. Chem. Soc.* **2001**, *123*, 4859.
(41) Yanagisawa, S.; Banfield, M. J.; Dennison, C. *Biochemistry* **2006**, *45*, 8812.
(42) Kataoka, K.; Hirota, S.; Maeda, Y.; Kogi, H.; Shinohara, N.; Sekimoto, M.; Sakurai, T. *Biochemistry* **2011**, *50*, 558.
(43) Machczynski, M. C.; Gray, H. B.; Richards, J. H. *J. Inorg. Biochem.* **2002**, *88*, 375.
(44) Carrell, C. J.; Sun, D.; Jiang, S.; Davidson, V. L.; Mathews, F. S. *Biochemistry* **2004**, *43*, 9372.
(45) Nishiyama, M.; Suzuki, J.; Ohnuki, T.; Chang, H. C.; Horinouchi, S.; Turley, S.; Adman, E. T.; Beppu, T. *Protein Eng.* **1992**, *5*, 177.
(46) Hall, J. F.; Kanbi, L. D.; Harvey, I.; Murphy, L. M.; Hasnain, S. S. *Biochemistry* **1998**, *37*, 11451.
(47) Kanbi, L. D.; Antonyuk, S.; Hough, M. A.; Hall, J. F.; Dodd, F. E.; Hasnain, S. S. *J. Mol. Biol.* **2002**, *320*, 263.
(48) Hoitink, C. W. G.; Canters, G. W. *J. Biol. Chem.* **1992**, *267*, 13836.
(49) Rose, K.; Shadle, S. E.; Eidsness, M. K.; Kurtz, D. M.; Scott, R. A.; Hedman, B.; Hodgson, K. O.; Solomon, E. I. *J. Am. Chem. Soc.* **1998**, *120*, 10743.
(50) Sun, N.; Dey, A.; Xiao, Z.; Wedd, A. G.; Hodgson, K. O.; Hedman, B.; Solomon, E. I. *J. Am. Chem. Soc.* **2010**, *132*, 12639.
(51) Kang, J.; Ohta, T.; Hagiwara, Y.; Nishikawa, K.; Yamamoto, T.; Nagao, H.; Tateno, M. *J. Phys.: Condens. Matter* **2009**, *21*, 064235/1.
(52) Chang, T. K.; Iverson, S. A.; Rodrigues, C. G.; Kiser, C. N.; Lew, A. Y. C.; Germanas, J. P.; Richards, J. H. *Proc. Natl. Acad. Sci. U.S.A.* **1991**, *88*, 1325.
(53) Mizoguchi, T. J.; Di Bilio, A. J.; Gray, H. B.; Richards, J. H. *J. Am. Chem. Soc.* **1992**, *114*, 10076.
(54) Hedman, B.; Frank, P.; Gheller, S. F.; Roe, A. L.; Newton, W. E.; Hodgson, K. O. *J. Am. Chem. Soc.* **1988**, *110*, 3798.
(55) Nurizzo, D.; Silvestrini, M.-C.; Mathieu, M.; Cutruzzola, F.; Bourgeois, D.; Fulop, V.; Hajdu, J.; Brunori, M.; Tegoni, M.; Cambillau, C. *Structure* **1997**, *5*, 1157.
(56) DeBeer George, S.; Metz, M.; Szilagyi, R. K.; Wang, H.; Cramer, S. P.; Lu, Y.; Tolman, W. B.; Hedman, B.; Hodgson, K. O.; Solomon, E. I. *J. Am. Chem. Soc.* **2001**, *123*, 5757.
(57) George, G. N. *EXAFSPAK & EDG_FIT*; Stanford Synchrotron Radiation Lightsource, SLAC National Accelerator Laboratory, Stanford University: Stanford, CA, 2000.
(58) Frisch, M. J.; et al. *Gaussian 09*, Revision B.01; Gaussian, Inc.: Wallingford, CT, 2009.
(59) Miertus, S.; Scrocco, E.; Tomasi, J. *Chem. Phys.* **1981**, *55*, 117.
(60) Tenderholt, A. L. *QMForge*, Version 2.1; Stanford University, Stanford, CA
(61) Kieber-Emmons, M. T. *Lumo*, Version 0.9b; Burlingame, CA, 2011.
(62) Gorelsky, S. I.; Lever, A. B. P. *J. Organomet. Chem.* **2001**, *635*, 187.
(63) Gorelsky, S. I. *SWizard* (http://www.sg-chem.net/); University of Ottawa, Ottawa, Canada, 2010.
(64) Becke, A. D. *J. Chem. Phys.* **1993**, *98*, 5648.
(65) Schaefer, A.; Huber, C.; Ahlrichs, R. *J. Chem. Phys.* **1994**, *100*, 5829.
(66) Francl, M. M.; Pietro, W. J.; Hehre, W. J.; Binkley, J. S.; Gordon, M. S.; DeFrees, D. J.; Pople, J. A. *J. Chem. Phys.* **1982**, *77*, 3654.
(67) Hariharan, P. C.; Pople, J. A. *Theor. Chim. Acta* **1973**, *28*, 213.
(68) Rassolov, V. A.; Pople, J. A.; Ratner, M. A.; Windus, T. L. *J. Chem. Phys.* **1998**, *109*, 1223.
(69) Bates, W. W.; Hobbs, M. E. *J. Am. Chem. Soc.* **1951**, *73*, 2151.
(70) Perdew, J. P. *Phys. Rev. B* **1986**, *33*, 8822.
(71) Becke, A. D. *Phys. Rev. A: Gen. Phys.* **1988**, *38*, 3098.
(72) Szilagyi, R. K.; Metz, M.; Solomon, E. I. *J. Phys. Chem. A* **2002**, *106*, 2994.
(73) Piepho, S. B.; Schatz, P. N. *Group Theory in Spectroscopy: With Applications to Magnetic Circular Dichroism*; John Wiley & Sons: New York, 1983.
(74) MCD intensities used for calculating the C_0/D_0 ratio were obtained in the region where the signal intensity is linear in both temperature and field.
(75) Siiman, O.; Young, N. M.; Carey, P. R. *J. Am. Chem. Soc.* **1974**, *96*, 5583.
(76) Miskowski, V.; Tang, S. P. W.; Spiro, T. G.; Shapiro, E.; Moss, T. H. *Biochemistry* **1975**, *14*, 1244.
(77) Siiman, O.; Young, N. M.; Carey, P. R. *J. Am. Chem. Soc.* **1976**, *98*, 744.
(78) Ferris, N. S.; Woodruff, W. H.; Tennent, D. L.; McMillin, D. R. *Biochem. Biophys. Res. Commun.* **1979**, *88*, 288.
(79) Thamann, T. J.; Frank, P.; Willis, L. J.; Loehr, T. M. *Proc. Natl. Acad. Sci. U.S.A.* **1982**, *79*, 6396.
(80) Blair, D. F.; Campbell, G. W.; Lum, V.; Martin, C. T.; Gray, H. B.; Malmström, B. G.; Chan, S. I. *J. Inorg. Biochem.* **1983**, *19*, 65.
(81) Woodruff, W. H.; Norton, K. A.; Swanson, B. I.; Fry, H. A. *J. Am. Chem. Soc.* **1983**, *105*, 657.

(82) Woodruff, W. H.; Norton, K.; Swanson, B. I.; Fry, H. A.; Malmström, B. G.; Pecht, I.; Blair, D. F.; Cho, W.; Campbell, G. W.; Lum, V.; Miskowski, V. M.; Chan, S. I.; Gray, H. B. *Inorg. Chim. Acta* **1983**, *79*, 51.
(83) Nestor, L.; Larrabee, J. A.; Woolery, G.; Reinhammar, B.; Spiro, T. G. *Biochemistry* **1984**, *23*, 1084.
(84) Woodruff, W. H.; Norton, K. A.; Swanson, B. I.; Fry, H. A. *Proc. Natl. Acad. Sci. U.S.A.* **1984**, *81*, 1263.
(85) Blair, D. F.; Campbell, G. W.; Cho, W. K.; English, A. M.; Fry, H. A.; Lum, V.; Norton, K. A.; Schoonover, J. R.; Chan, S. I. *J. Am. Chem. Soc.* **1985**, *107*, 5755.
(86) Han, J.; Adman, E. T.; Beppu, T.; Codd, R.; Freeman, H. C.; Huq, L.; Loehr, T. M.; Sanders-Loehr, J. *Biochemistry* **1991**, *30*, 10904.
(87) DSarangi, R.; Gorelsky, S. I.; Basumallick, L.; Hwang, H. J.; Pratt, R. C.; Stack, T. D. P.; Lu, Y.; Hodgson, K. O.; Hedman, B.; Solomon, E. I. *J. Am. Chem. Soc.* **2008**, *130*, 3866.
(88) Dey, A.; Green, K. N.; Jenkins, R. M.; Jeffrey, S. P.; Darensbourg, M.; Hodgson, K. O.; Hedman, B.; Solomon, E. I. *Inorg. Chem.* **2007**, *46*, 9655.
(89) Schutz, C. N.; Warshel, A. *Proteins: Struct., Funct., Bioinf.* **2004**, *55*, 711.
(90) Dey, A.; Okamura, T.; Ueyama, N.; Hedman, B.; Hodgson, K. O.; Solomon, E. I. *J. Am. Chem. Soc.* **2005**, *127*, 12046.
(91) Dey, A.; Jenney, F. E., Jr.; Adams, M. W. W.; Johnson, M. K.; Hodgson, K. O.; Hedman, B.; Solomon, E. I. *J. Am. Chem. Soc.* **2007**, *129*, 12418.
(92) Dey, A.; Jiang, Y.; Ortiz, d., M. P.; Hodgson, K. O.; Hedman, B.; Solomon, E. I. *J. Am. Chem. Soc.* **2009**, *131*, 7869.
(93) Dey, A.; Hocking, R. K.; Larsen, P.; Borovik, A. S.; Hodgson, K. O.; Hedman, B.; Solomon, E. I. *J. Am. Chem. Soc.* **2006**, *128*, 9825.
(94) Comba, P.; Lledos, A.; Maseras, F.; Remenyi, R. *Inorg. Chim. Acta* **2001**, *324*, 21.
(95) Florian, J.; Warshel, A. *J. Phys. Chem. B* **1997**, *101*, 5583.
(96) Luzhkov, V.; Warshel, A. *J. Comput. Chem.* **1992**, *13*, 199.
(97) δ is calculated using the energy of the S(thiolate)-based 3p orbital in the reduced state of the BC model with active and passive H-bonds at 3.5 Å.
(98) Kamerlin, S. C. L.; Warshel, A. *Wiley Interdiscip. Rev.: Comput. Mol. Sci.* **2011**, *1*, 30.
(99) Warshel, A.; Weiss, R. M. *J. Am. Chem. Soc.* **1980**, *102*, 6218.
(100) Lancaster, K. In *Structucture and Bonding (Berlin)*; Mingos, D. M. P., Day, P., Dahl, J. P., Eds.; Springer: Berlin/Heidelberg, 2012; Vol. *142*.